LAWRENCE
LIVERMORE
NATIONAL
LABORATORY

LLNL-JRNL-656795

Kinetic Simulations and Reduced Modeling of Longitudinal Sideband Instabilities in Non-Linear Electron Plasma Waves

S. Brunner, R. L. Berger, B. I. Cohen, L. Hausammann, E. J. Valeo

July 8, 2014

Physics of Plasmas

Disclaimer

LLNL-JRNL-656795

Kinetic Simulations and Reduced Modeling of Longitudinal Sideband Instabilities in Non-Linear Electron Plasma Waves

S. Brunner[1],* R. L. Berger[2],† B. I. Cohen[2], L. Hausammann[1], and E. J. Valeo[3]

(1) Centre de Recherches en Physique des Plasmas,

Association Euratom-Confédération Suisse,

Ecole Polytechnique Fédérale de Lausanne,

CRPP-PPB, CH-1015 Lausanne, Switzerland

(2) Lawrence Livermore National Laboratory,

University of California, P.O. Box 808,

Livermore, California 94551, USA and

(3) Princeton Plasma Physics Laboratory, P.O. Box 451,

Princeton, New Jersey 08543, USA-0451

(Dated: October 8, 2014)

Abstract

Kinetic Vlasov simulations of one-dimensional finite amplitude Electron Plasma Waves (EPWs) are performed in a multi-wavelength long system. A systematic study of the most unstable linear sideband mode, in particular its growth rate γ and quasi- wavenumber δk, is carried out by scanning the amplitude and wavenumber of the initial wave. Simulation results are successfully compared against numerical and analytical solutions to the reduced model by Kruer [W. L. Kruer *et al.*, Phys. Rev. Lett. **23**, 838 (1969)] for the Trapped Particle Instability (TPI). A model recently suggested by Dodin [I. Y. Dodin *et al.*, Phys. Rev. Lett. **110**, 215006 (2013)], which in addition to the TPI accounts for the so-called Negative Mass Instability (NMI) because of a more detailed representation of the trapped particle dynamics, is also studied and compared with simulations.

*stephan.brunner@epfl.ch

†berger5@llnl.gov

I. INTRODUCTION

In laser-fusion plasmas, parametric instabilities affecting the propagation of the incident laser light are of great concern. Among these, one distinguishes Stimulated Raman Scattering (SRS) as well as Stimulated Brillouin Scattering (SBS), which respectively result from the scattering of laser light off of an Electron Plasma Wave (EPW) or an Ion Acoustic Wave (IAW). The deleterious effect from parametric instabilities results from the often significant fraction of reflected laser light and associated loss of target drive, as well as, in the case of SRS, from the possible generation of energetic electrons which can pre-heat the target.

Kinetic simulations have shown that sideband instabilities, breaking up the finite amplitude Electron Plasma Waves (EPWs), provide a potential saturation mechanism for SRS in inertial-fusion related plasmas. This has been demonstrated both in spatially one-dimensional Eulerian simulations [1, 2], involving longitudinal sidebands, as well as in spatially two-dimensional PIC simulations [3–5], involving transverse sidebands (filamentation). The Langmuir Decay Instability (LDI) in which the SRS-driven EPW scatters from an IAW into a counter-propagating EPW is another potential saturation process.[6, 7].

Kruer, Dawson, and Sudan provided a simple but elegant reduced model (further referred to as KDS) for describing the mechanism of the Trapped Particle Instability (TPI) [8]. The TPI involves the resonant interaction between trapped electrons in an initially large-amplitude EPW and sideband modes. This interaction leads to an effective transfer of energy from the original EPW to the resonant sidebands and thus to their destabilization. Despite its simplicity, the KDS model appeared to be successful in providing at least a semi-quantitative agreement with EPW sideband growth rates diagnosed in SRS simulations [1].

The goal of this paper is to present a more systematic study of the longitudinal EPW sideband instability dynamics, in particular its linear evolution, achieved by analyzing a series of dedicated 1+1-dimensional (one configuration space dimension + one velocity space dimension) kinetic simulations over a range of wave amplitudes $e\phi_L/T_e$ and wavenumbers $k_L\lambda_{De}$ of the initial Large-Amplitude Wave (LAW). Here ϕ_L stands for the electrostatic potential associated with the LAW, T_e for the electron temperature, e for the elementary charge, and λ_{De} for the electron Debye length. Simulations have been carried out with the SAPRISTI code [9, 10]. SAPRISTI solves the Vlasov-Poisson system considering an Eulerian representation for the phase-space distribution of each plasma species and applying a semi-Lagrangian

scheme for carrying out its time evolution, as originally presented in [11]. Eulerian-type simulations (also called grid-based) have the advantage over the Particle-In-Cell (PIC) approach in providing noise-free and thus numerically very clean results, particularly well adapted for analyzing the low amplitude, linear phase of instabilities.

It will be shown that the agreement between the KDS model and kinetic simulation results reported in Ref. [1] for a particular set of parameters can in fact be confirmed over a wide range of wave amplitudes and wavenumbers. The ranges considered for these parameters are respectively $0 < e\phi_L/T_e \lesssim 1$ and $0.25 < k_L\lambda_{De} < 0.45$. The detailed analysis of the simulation results in particular confirms the Bloch-Floquet -type nature of sidebands predicted by theory, which is the origin of the characteristic symmetric, double-humped form of the sideband growth rate spectrum. This spectrum is compared to the one predicted by the reduced KDS model, with remarkably good agreement given the simplicity of KDS.

A more recent reduced model for describing instabilities affecting a LAW has been proposed by Dodin [12], providing a somewhat more detailed description of the trapped particle dynamics than the KDS model. In addition to the TPI, the Dodin model also accounts for the so-called Negative Mass Instability (NMI). The NMI is a consequence of the reduction of the bounce frequency of less deeply trapped particles compared to deeply trapped ones, potentially leading to the bunching of particles in their phase-space rotation. Whether the simulation results present any trace of the NMI has therefore been investigated as well.

The remainder of this paper is organized as follows: The KDS model is briefly summarized in Sec. II. Numerical solutions to the sideband dispersion relation in the context of the KDS model are presented and discussed in Sec. III. Such a solution is shown in Fig. 1, clearly illustrating how the TPI results from a resonance in the frame of the initial wave between the Doppler-shifted frequency of the sideband and the bounce frequency of trapped particles. Based on these "exact" results, a practical analytical solution to the KDS model for the most unstable sideband is derived in Sec. IV. The Dodin model is discussed and solutions to its dispersion relation compared to KDS in Sec. V. Figures 5 and 6, for example, illustrate how the solution to the dispersion relation from the Dodin model contains additional unstable branches associated to the NMI. The TPI branches remain however the most unstable and essentially unchanged compared to the solutions from the KDS model. The kinetic simulations carried out with the SAPRISTI code are presented in Sec. VI. A short description of the code is provided in VI A, and a typical simulation

result of sideband instabilities affecting a large-amplitude EPW is analyzed in detail in VI B, including comparisons with the KDS and Dodin model predictions. The time evolution of the Fourier spectrum of the sidebands is plotted in Figs. 8 and 9, providing a clear illustration of the perfectly symmetric growth of upper and lower sidebands throughout their *linear* phase of evolution, as predicted by theory. The real frequency and growth rate spectra of the sidebands obtained from the simulation are compared to the reduced models in Fig. 11, with very good agreement with respect to the most unstable TPI modes. Results of a study of the sideband instability for an extensive scan over wavenumber $k_L\lambda_{De}$ and amplitude $e\phi_L/T_e$ of the LAW are presented in Sec. VI C. This scan is summarized in Fig. 16, where the growth rate and associated wavenumber of the most unstable sideband obtained from the simulation are compared to the theory for all cases considered. Conclusions are drawn and comparison of the longitudinal sideband to the transverse sideband and the LDI growth rates are made in Sec. VII. The paper ends with two appendices. Appendix A provides details to the trapped particle fraction estimation, a key parameter in the reduced sideband models, in two limiting cases of generation of the LAW: "sudden" and "adiabatic". Appendix B presents a systematic derivation of the KDS and Dodin models from the general linear kinetic formalism by Goldman for the stability analysis of LAWs [13]. With this explicit derivation the numerous approximations underlying the reduced models are elucidated.

II. THE KDS MODEL

The KDS model [8] provides a linear stability analysis of a large-amplitude, periodic EPW to sideband modes. Here, k_L, ω_L, and $v_L = \omega_L/k_L$ will respectively stand for the wavenumber, frequency and phase velocity of the LAW in the laboratory frame. We assume that the LAW is essentially stationary in the wave frame, therefore corresponding to a BGK-type mode [14]. In this moving frame, the unperturbed system is thus spatially periodic and time independent, so that the linear eigenmodes resulting from the stability analysis are expected to be of Bloch-Floquet -type, *i.e.* with fixed frequency $\delta\omega'_S$ and coupling spatial Fourier modes with wavenumbers $k_{S,n} = \delta k_S + nk_L$, $n = 0, \pm1, \pm2, \ldots$. The general theory for the stability analysis of LAWs has been derived by Goldman in [13]. Although formally exact, its implementation in practical cases is not straightforward. As shown in [13] and recalled in Appendix B, the KDS model is in fact an approximate derivation of the general

Goldman formulation, assuming that only the dynamics of trapped particles are affected by the presence of the LAW, while all other particles (bulk of the distribution) still respond as in an homogeneous plasma. In this reduced model it is thus only the trapped electrons which couple the different Fourier modes $k_{S,n}$ of a Floquet-type sideband mode and lead to its destabilization. The KDS model makes the further simplification of representing all the trapped particles in a given potential well of the LAW by a single macro-particle, assumed to carry out a harmonic oscillation with bounce frequency ω_B. In this reduced representation, the following system of equations is obtained for the Fourier components of the sideband mode:

$$\epsilon(k,\omega)\delta\hat{E}(k,\omega) = \frac{\omega_t^2}{(\omega - k\,v_L)^2 - \omega_B^2} \sum_{n=-\infty}^{+\infty} \delta\hat{E}(k + nk_L, \omega + n\omega_L), \tag{1}$$

where $\delta\hat{E}(k,\omega)$ is the Fourier component with wavenumber k and laboratory frame frequency ω of the electrostatic field associated with the sideband. The background response is represented by the dielectric function $\epsilon(k,\omega)$ of the homogeneous plasma, which in the KDS model is approximated by the following fluid relation:

$$\epsilon(k,\omega) = 1 - \frac{\omega_{pe}^2}{\omega^2 - 3(kv_{\mathrm{th,e}})^2}, \tag{2}$$

with $\omega_{pe}^2 = N_e e^2/(m_e\epsilon_0)$ the electron plasma frequency squared, $v_{\mathrm{th,e}}^2 = T_e/m_e$ the electron thermal velocity squared, N_e and T_e the background electron density and temperature respectively. Here m_e is the electron mass and ϵ_0 is the electric permittivity of free space. Note that the dielectric function (2) assumes fixed ions, which is a well-justified approximation for describing EPWs.

Equation (1) represents the coupling of Fourier modes $(k_{S,n}, \omega_{S,n})$, with $k_{S,n} = \delta k_S + nk_L$ and $\omega_{S,n} = \delta\omega_S + n\omega_L$, where the so-called quasi-wavenumber δk_S can be chosen within the first Brillouin zone, *i.e.* $|\delta k_S/k_L| < 1/2$. Note that in the LAW frame, the Doppler shifted frequencies for these different coupled Fourier modes reduces to a single frequency, $\delta\omega'_S$ mentioned above, thus confirming the functional form of a Bloch-Floquet mode: $\delta\omega'_S = \omega_{S,n} - k_{S,n}v_L = \delta\omega_S - \delta k_S v_L$.

The coupling between the Fourier modes is provided by the coefficient

$$C = \frac{\omega_t^2}{(\omega - k\,v_L)^2 - \omega_B^2}. \tag{3}$$

As $\omega - k\,v_L = \delta\omega'_S$, the denominator approaches zero when the (real) frequency of the sideband mode in the moving frame matches the bounce frequency $\delta\omega'_{S,r} = \pm\omega_B$, reflecting

a possible resonant interaction with the trapped particles. It will be shown in Sec. III that the most unstable sideband closely verifies this resonant condition.

The basic parameter in Eq. (1) providing the coupling between Fourier modes is the plasma frequency squared of the trapped electrons, $\omega_t^2 = N_t e^2/(m_e \epsilon_0) = f_t\, \omega_{pe}^2$, having noted $N_t = f_t\, N_e$ the spatially averaged density of trapped electrons and f_t the trapped fraction. This clearly reflects that the Fourier mode coupling in the KDS model is essentially provided by the trapped particles.

The fraction of trapped particles f_t, as well as the bounce frequency ω_B, depend on the amplitude ϕ_L of the LAW; more details about how these parameters are estimated are provided in Sec. III. In any case, for vanishing ϕ_L, one has $\omega_t \to 0$, and Eq. (1) provides, as expected, the linear dispersion relation for EPWs in an homogeneous plasma, which together with the fluid dielectric function (2) leads to the well-known Bohm-Gross dispersion relation for a single Fourier mode $\delta\hat{E}(k, w)$:

$$\epsilon(k, \omega) = 0 \qquad \Longrightarrow \qquad \omega^2 = \omega_{pe}^2 + 3(k v_{\mathrm{th,e}})^2. \tag{4}$$

Equation (1) in fact states (the right side being independent of n) that the Fourier modes $\delta\hat{E}(k_{S,n}, \omega_{S,n})$ composing a sideband are such that

$$\epsilon(k_{S,n}, \omega_{S,n})\, \delta\hat{E}(k_{S,n}, \omega_{S,n}) = \mathrm{const.} \tag{5}$$

The dominant Fourier components in the Bloch-Floquet mode are thus those which are nearest to verifying the linear dispersion relation for waves in an homogeneous plasma:

$$\epsilon(k_{S,n}, \omega_{S,n}) \simeq 0 \qquad \Longrightarrow \qquad \omega_{S,n} = \delta\omega_S + n\omega_L \simeq \pm\omega_{pe}. \tag{6}$$

As the LAW is also an EPW, one has $\omega_L \simeq \omega_{pe}$. Furthermore, expecting $|\delta\omega_S/\omega_L| \ll 1$ up to moderate coupling of the Fourier components, *i.e.* moderate normalized initial wave amplitudes $e\phi_L/T_e$, only the two Fourier components $n = \pm 1$ can satisfy the approximate condition (6). Under this argument, the KDS model furthermore restricts the representation of sideband modes to these two components, leading to the following rank 2 eigenvalue problem:

$$\mathbf{M} \cdot \begin{pmatrix} \delta\hat{E}_{+1} \\ \delta\hat{E}_{-1} \end{pmatrix} = 0, \tag{7}$$

with

$$\mathbf{M} = \begin{pmatrix} \epsilon_{+1} - C & -C \\ -C & \epsilon_{-1} - C \end{pmatrix}, \tag{8}$$

having used the compact notation $\delta\hat{E}_n = \delta\hat{E}(k_{S,n}, \omega_{S,n})$ and $\epsilon_n = \epsilon(k_{S,n}, \omega_{S,n})$. The wavenumber-frequency pair $(\delta k_S, \delta\omega_S)$, characterizing a given Bloch-Floquet sideband mode, must therefore be such that

$$\det(\mathbf{M}) = \epsilon_{+1}\epsilon_{-1} - C\left(\epsilon_{+1} + \epsilon_{-1}\right) = 0, \tag{9}$$

which provides the TPI dispersion relation. In case $\epsilon_{\pm 1} \neq 0$, Eq. (9) can also be written:

$$1 = C\left(\frac{1}{\epsilon_{+1}} + \frac{1}{\epsilon_{-1}}\right). \tag{10}$$

The corresponding sideband mode structure, *i.e.* eigenvector, is composed of the Fourier components $\delta\hat{E}_{\pm 1}$ with relative amplitudes, according to (5), such that

$$\frac{\delta\hat{E}_{+1}}{\delta\hat{E}_{-1}} = \frac{\epsilon_{-1}}{\epsilon_{+1}}. \tag{11}$$

The dispersion relation (10) verifies certain symmetry properties. In general (even in a kinetic description), the dielectric function must verify the relation

$$\epsilon(k, \omega) = \epsilon^\star(-k, -\omega^\star), \tag{12}$$

where $\star$ stands for the complex conjugate. Using relation (12), one can easily derive from (7)-(10) that if $(\delta k_S, \delta\omega_S)$ is a solution to the TPI dispersion relation with associated eigenvector $(\delta\hat{E}_{+1}, \delta\hat{E}_{-1})$, then $(-\delta k_S, -\delta\omega_S^\star)$ is a solution as well with associated eigenvector $(\delta\hat{E}_{-1}^\star, \delta\hat{E}_{+1}^\star)$. These symmetry relations just mentioned are simply related to the reality condition which the (physical) solutions must verify. The fluid dielectric function (2) considered by the KDS model obviously verifies (12), but verifies as well

$$\epsilon(k, \omega) = \epsilon^\star(k, \omega^\star). \tag{13}$$

As a result, if $(\delta k_S, \delta\omega_S)$ is a solution to (10) with associated eigenvector $(\delta\hat{E}_{+1}, \delta\hat{E}_{-1})$, $(\delta k_S, \delta\omega_S^\star)$ is a solution as well with associated eigenvector $(\delta\hat{E}_{+1}^\star, \delta\hat{E}_{-1}^\star)$, *i.e.* solutions appear in conjugate complex pairs, as expected for a fluid-like dispersion relation.

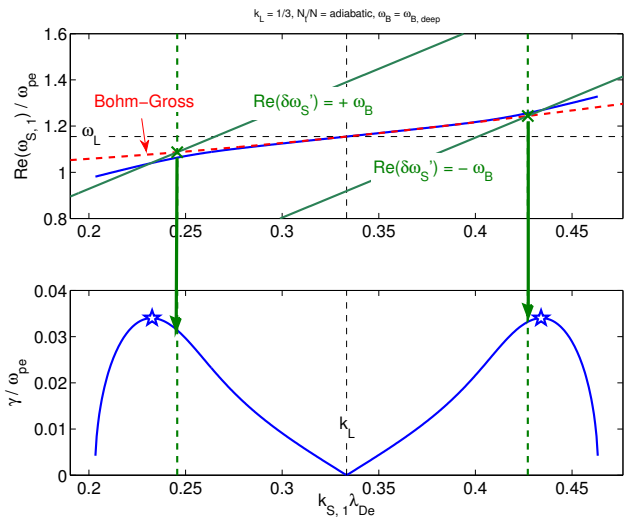

FIG. 1: (Color online) Example of numerical solution to the KDS dispersion relation. Considering a LAW with $k_L\lambda_{De} = 0.333$ and $e\phi_L/T_e = 0.5$. The real frequency $\omega_L/\omega_{pe} = 1.155$ is estimated from the Bohm-Gross (linear, fluid) relation. The fraction of trapped particles is chosen adiabatic, $N_t^{\rm ad}/N = 5.17 \cdot 10^{-3}$, and the bounce frequency $\omega_B = \omega_{B,\rm deep} = 0.236\,\omega_{pe}$. The top plot shows (in blue) the real frequency $\mathrm{Re}(\omega_{S,1})$ and the bottom plot the growth rate $\gamma = \mathrm{Im}(\omega_{S,1})$ of the most unstable root in units of ω_{pe} as a function of the wavenumber $k_{S,1}\lambda_{De}$ of the Fourier component $n = 1$ composing the sideband. The real frequency of free EPWs from the Bohm-Gross dispersion relation (in red) as well as the resonance condition $\mathrm{Re}(\delta\omega_S') = \mathrm{Re}(\omega_{S,1}) - k_{S,1}v_L = \pm\omega_B$ (in green) are also shown.

III. NUMERICAL SOLUTION TO THE KDS MODEL

The dispersion relation (10) for the TPI considering the dielectric function (2) leads to a polynomial equation of degree 6 for the normalized complex frequency $\delta\omega_S/\omega_{pe}$ as a function of the normalized wavenumber $\delta k_S\lambda_{De}$, which can be solved numerically. The parameters appearing in the dispersion relation (10) and characterizing the LAW are its normalized wavenumber $k_L\lambda_{De}$, normalized frequency ω_L/ω_{pe}, the fraction of trapped particles $f_t = N_t/N$ and the normalized bounce frequency ω_B/ω_{pe}.

Consistent with the true limit of the KDS model (see Sec. B 2), the bounce frequency is chosen as the frequency of deeply trapped particles given by relation $(\omega_{B,\rm deep}/\omega_{pe})^2 = (k_L\lambda_{De})^2(e\phi_L/T_e)$, assuming that the LAW is still essentially sinusoidal, which is a good

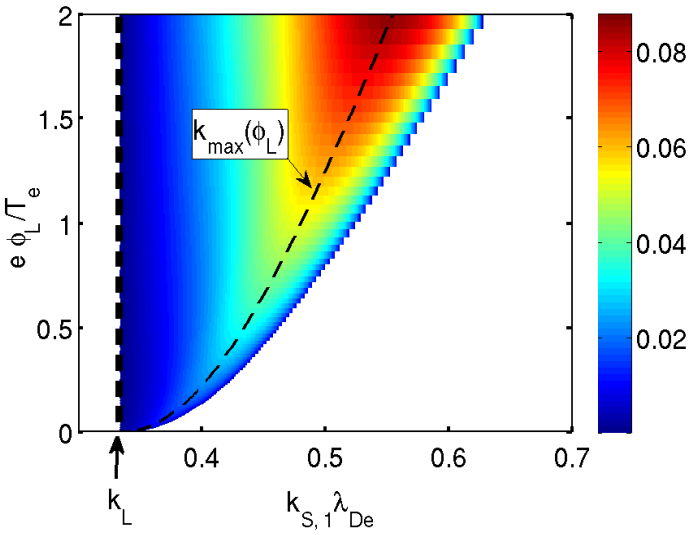

FIG. 2: Solution to the KDS dispersion relation for an amplitude scan of the LAW with $k_L\lambda_{De} = 0.333$. The growth rate γ/ω_{pe} of the unstable sideband is shown as a function of both the amplitude $e\phi_L/T_e$ of the LAW and the wavenumber $k_{S,1}\lambda_{De}$ of the Fourier component $n = 1$ composing the sideband (as γ is symmetric around k_L, only solutions for $k_{S,1} > k_L$ are plotted). The fraction of trapped particles $f_t(\phi_L) = N_t/N$ is again estimated with the adiabatic relation and the bounce frequency is set to $\omega_B(\phi_L) = \omega_{B,\text{deep}}$. For each amplitude ϕ_L the wavenumber $k_{\max}$ has been identified for which the growth rate is maximum (dashed black curve).

approximation for EPWs up to large amplitudes as harmonics are non-resonant and thus remain relatively small.

The fraction of trapped particles, $f_t = N_t/N$, not only depends on the amplitude ϕ_L, but also on how the LAW was generated. The two limiting cases of "sudden" and "adiabatic" generation [15] have been considered in Appendix A, providing two different estimates for f_t, as given by Eqs. (A1) and (A2) respectively for an initial Maxwellian electron distribution, $f_0 = f_M$. Results shown in Fig. 17.a illustrate that the adiabatic estimate for f_t is in very close agreement with the fraction of trapped particles computed in the kinetic simulations, especially when the phase velocity v_L of the LAW, required for estimating f_t, is evaluated using the *kinetic* dispersion relation [$v_L = \text{Re}(\omega)/k_L$, with the complex frequency ω solution to Eq. (A3)]. However, in the spirit of simplicity, most of the following results to the reduced KDS and Dodin model have been obtained with f_t estimated using v_L from the *fluid* (Bohm-Gross) dispersion relation (4), despite the fact that the agreement with the trapped

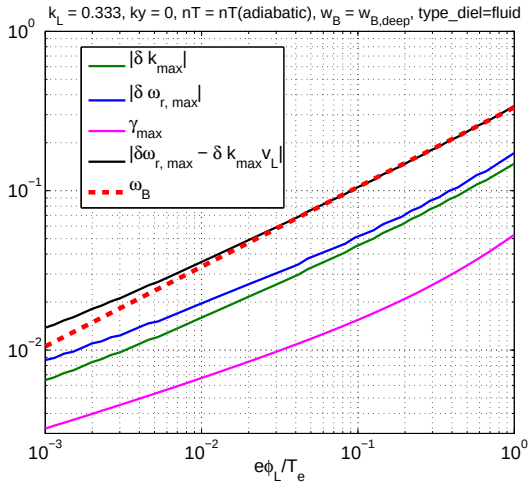

FIG. 3: Same amplitude scan at $k_L\lambda_{De} = 0.333$ as in Fig. 2. Plotting in log-log scale $|\delta k_{\max}| = |k_{\max} - k_L|$ (green, units λ_{De}^{-1}), $|\delta\omega_{r,\max}| = |\mathrm{Re}[\omega_{S,1}(k_{\max}) - \omega_L]|$ (blue, units ω_{pe}), and $\gamma_{\max} = \mathrm{Im}[\omega_{S,1}(k_{\max})]$ (magenta, units ω_{pe}) of most unstable sideband as a function of $e\phi_L/T_e$. Also shown is the wave frame sideband frequency $|\mathrm{Re}(\delta\omega'_S)| = |\delta\omega_{r,\max} - \delta k_{\max} v_L|$ (black), showing close resonance with ω_B (red) over a very wide range of amplitudes.

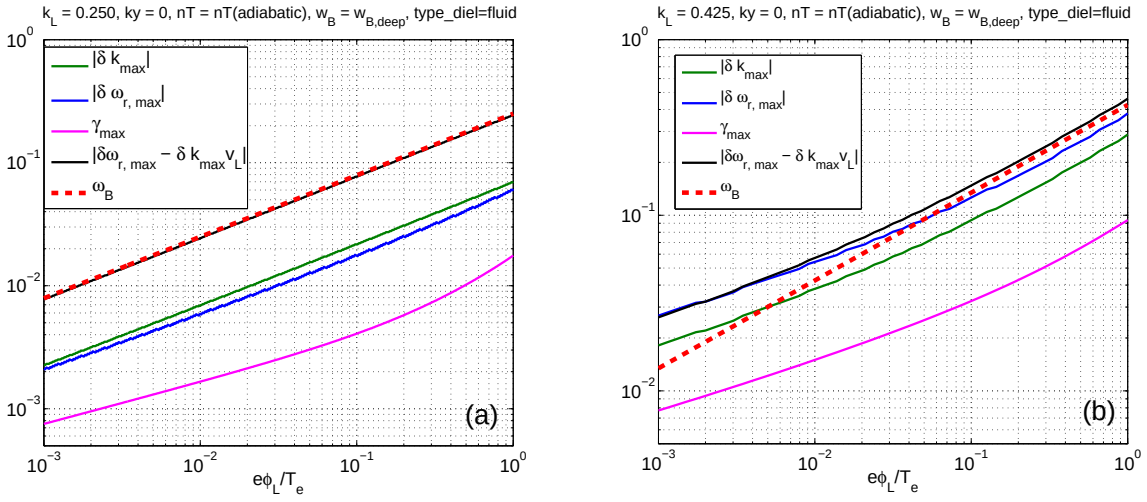

FIG. 4: Similar as Fig. 3 but for (a) $k_L\lambda_{De} = 0.250$, and (b) $k_L\lambda_{De} = 0.425$.

fractions from the simulations is not as close (see as well Fig. 17.a). In any case, this choice has no influence on the qualitative nature of the solutions to the reduced KDS and Dodin model studied in this section as well as in Sec. V. In Section VI C, where simulation and theoretical results for an extensive parameter scan are compared, the sensitivity of the

solution to the KDS model with respect to these different possible estimates of the adiabatic trapped fraction is discussed.

The appropriate choice for the frequency ω_L of the LAW with wavenumber k_L to be considered in the KDS model is a somewhat tricky issue. As discussed in Appendix B, section B 3, the exact linear spectrum of sidebands should contain the solution $(\delta k_S, \delta\omega'_S) = (0, 0)$. Demanding the KDS dispersion relation to satisfy this property, despite its numerous underlying approximations (see detailed discussion in Sec. B 2), leads to a condition on (k_L, ω_L) which appears as an effective dispersion relation for the LAW. Two possible equations in fact result from this constraint, either the linear dispersion relation

$$\epsilon(k_L, \omega_L) = 0, \tag{14}$$

leading to the Bohm-Gross relation (4), or the effective non-linear dispersion relation

$$\epsilon(k_L, \omega_L) = -2\frac{\omega_t^2}{\omega_B^2}, \tag{15}$$

leading to the non-linearly modified relation (B37) (setting $\alpha_0 = 0$, consistent with the KDS model considered here) and providing the non-linear frequency shift

$$\frac{\delta\omega_L}{\omega_{pe}} \simeq -\frac{\omega_t^2}{\omega_B^2}. \tag{16}$$

Equation (15) has in fact also been obtained through an alternative derivation in Ref. [16], but under the same assumption of deeply trapped particles as considered in the KDS model. One may point out that in Ref. [16] it is shown that to obtain relation (15) one in fact must assume $|\omega_t^2/\omega_B^2| \ll 1$ (this is indeed the case down to very low amplitudes for most cases of interest as shown in Fig. 17.b). Strictly speaking, the non-linear dispersion relation (15) is the "correct" one to be considered for (k_L, ω_L) as it yields a non-linear frequency shift, as expected for a finite-amplitude wave, which in addition is consistent with the KDS model. However, the resulting non-linear frequency shift (16) scales as $\sim \phi_L^{-1/2}$ for $\phi_L \to 0$ (as $\omega_t^2 \sim N_t \sim \phi_L^{1/2}$ and $\omega_B^2 \sim \phi_L$ in this limit), clearly in contradiction with more accurate models for non-linear frequency shifts resulting from trapping [15, 17] and confirmed by kinetic simulations [10], predicting a scaling $\sim \phi_L^{+1/2}$. In the following, it will be shown that choosing ω_L as verifying the linear Bohm-Gross dispersion relation leads to solutions to the KDS model which are in good semi-quantitative agreement with simulation results for the sideband instabilities, while considering ω_L according to the non-linear dispersion

relation (15) leads to predicted sideband growth rates which significantly overestimate the corresponding simulation results. In a somewhat pragmatic spirit we therefore have mainly considered the linear solution for ω_L.

A typical example of solution to the KDS TPI dispersion relation (10) is shown in Fig. 1 for a LAW with wavenumber $k_L\lambda_{De} = 0.333$ and amplitude $e\phi_L/T_e = 0.5$. The frequency $\omega_L/\omega_{pe} = 1.155$ was estimated from the Bohm-Gross dispersion relation. The fraction of trapped particles was evaluated with the adiabatic relation (A2) and using the fluid estimate $v_L/v_{\mathrm{th,e}} = 3.464$, providing $N_t^{\mathrm{ad}}/N = 5.17 \cdot 10^{-3}$, and the bounce frequency computed with the relation for deeply trapped particles, $\omega_B = \omega_{B,\mathrm{deep}} = 0.236\,\omega_{pe}$. Both the real frequency $\mathrm{Re}(\omega_{S,1})$ and growth rate $\gamma = \mathrm{Im}(\omega_{S,1})$ are plotted as a function of the corresponding Fourier component wavenumber $k_{S,1}$. Notice the double-humped solution for $\gamma(k_{S,1})$ centered around $k_{S,1} = k_L$, revealing the even dependence of γ with respect to $\delta k_S = k_{S,1} - k_L$, as well as the odd dependence of $\mathrm{Re}(\delta\omega_S) = \mathrm{Re}(\omega_{S,1}) - \omega_L$ with respect to δk_S, clearly the result of the symmetry properties of the dispersion relation discussed in Sec. II. Remarkable as well from Fig. 1: 1) the real frequencies $\mathrm{Re}(\omega_{S,n})$ of the sideband Fourier components $n = \pm 1$ closely follow the linear dispersion relation of free EPWs provided by the Bohm-Gross dispersion relation (4) (blue and dashed red curves closely overlap), and 2) the wavenumbers of the most unstable sidebands (corresponding growth rates highlighted with blue stars) are well approximated by the intersection points between the Bohm-Gross dispersion relation and the resonance condition $\mathrm{Re}(\delta\omega'_S) = \mathrm{Re}(\omega_{S,1}) - k_{S,1}v_L = \pm\omega_B$ (green crosses). These two last points will be invoked for deriving an analytical solution to the KDS dispersion relation in Sec. IV.

The numerical solution to the KDS dispersion relation for an amplitude scan of the LAW, still considering $k_L\lambda_{De} = 0.333$ as well as the adiabatic trapped fraction $f_t(\phi_L) = N_t^{\mathrm{ad}}/N$ and $\omega_B(\phi_L) = \omega_{B,\mathrm{deep}}$ (obviously both varying with amplitude), is shown in Fig. 2. Plotted is the growth rate γ of the unstable sideband as a function of both the amplitude $e\phi_L/T_e$ of the LAW and the wavenumber $k_{S,1}\lambda_{De}$ of the Fourier component $n = 1$ composing the sideband eigenmode. For each amplitude ϕ_L, the maximum sideband growth rate $\gamma_{\max} = \max_{k_{S,1}}(\gamma)$ and corresponding real frequency $|\delta\omega_{r,\max}| = |\mathrm{Re}(\omega_{S,1} - \omega_L)|$ and wavenumber $|\delta k_{\max}| = |k_{S,1} - k_L|$ have been reported in the log-log plot shown in Fig. 3. These results from the KDS model clearly illustrate how $|\delta k_{\max}|$, $|\delta\omega_{r,\max}|$, and $\gamma_{\max}$ all converge to zero as $\phi_L \to 0$. Also illustrated in Fig. 3 is how the resonance condition $|\mathrm{Re}(\delta\omega'_S)| = |\delta\omega_{r,\max} - \delta k_{\max}v_L| = \omega_B$

is closely maintained down to very low amplitudes. Similar numerical solutions to the KDS model along amplitude scans are shown in Figs. 4.a and 4.b for LAWs with $k_L\lambda_{De} = 0.250$ and $k_L\lambda_{De} = 0.425$ respectively.

IV. ANALYTICAL SOLUTION TO THE KDS MODEL

As already mentioned, the dispersion relation (9) for the sideband modes in the frame of the KDS model, together with the fluid relation (2) for the dielectric function, leads to a polynomial equation of degree 6 for the frequency $\delta\omega_S/\omega_{pe}$, which in its general form cannot be solved exactly. Despite the fact that this equation is straightforward to solve numerically, as shown in Sec. III, an analytic relation, even approximate, can be desirable for obtaining quick estimates, as well as for providing further insight into how the various parameters, in particular the trapped fraction f_t and the bounce frequency ω_B, influence the instability growth rates. The goal here is to derive such an approximate analytical relation for the most unstable solution to the dispersion relation given by Eq. (9). To this end, we shall be guided by the properties exhibited by the numerical solutions presented in Sec. III.

Appearing in Eq. (9) are the terms $\epsilon_{\pm 1} = \epsilon(k_{S,\pm 1}, \omega_{S,\pm 1})$. Invoking the fact that the frequencies $\omega_{S,\pm 1}$ of the most unstable sidebands are close to the dispersion relation of free EPWs (as illustrated in Fig. 1), the terms $\epsilon_{\pm 1}$ are approximated as follows:

$$\begin{aligned}\epsilon_{\pm 1} &= \epsilon(k_{S,\pm 1}, \omega_{S,\pm 1}) = \epsilon(k_{S,\pm 1}, \omega_{k_{S,\pm 1}} + \omega_{S,\pm 1} - \omega_{k_{S,\pm 1}}) \\ &\simeq (\omega_{S,\pm 1} - \omega_{k_{S,\pm 1}}) \left.\frac{\partial \epsilon}{\partial \omega}\right|_{(k_{S,\pm 1}, \omega_{k_{S,\pm 1}})},\end{aligned} \tag{17}$$

having Taylor expanded $\epsilon(k_{S,\pm 1}, \omega)$ to first order with respect to $\omega = \omega_{k_{S,\pm 1}}$, where ω_k stands for the actual solution to the homogeneous plasma dispersion relation for wavenumber k, $\epsilon(k, \omega_k) = 0$. Furthermore, as $k_{S,\pm 1} = \delta k_S \pm k_L$ with $|\delta k_S/k_L| \ll 1$ for the unstable sidebands (at least up to moderate values of $e\phi_L/T_e$), $\omega_{k_{S,\pm 1}}$ can itself be Taylor expanded. Considering terms up to second order, one thus obtains:

$$\begin{aligned}\omega_{k_{S,\pm 1}} &= \pm\omega_{k_L \pm \delta k_S} \\ &\simeq \pm \left(\omega_{k_L} \pm \left.\frac{d\omega}{dk}\right|_{k_L} \delta k_S + \frac{1}{2} \left.\frac{d^2\omega}{dk^2}\right|_{k_L} \delta k_S^2 \right) \\ &= \pm\,\omega_L + v_g \delta k_S \pm \frac{1}{2} D \delta k_S^2,\end{aligned} \tag{18}$$

having made use of $\omega_{-k} = -\omega_k$, $\omega_L = \omega_{k_L}$, and the notation $v_g = d\omega/dk|_{k_L}$ for the group velocity, as well as $D = d^2\omega/dk^2|_{k_L}$ for the dispersion. Combining Eqs. (17) and (18) then leads to

$$\begin{aligned}\epsilon_{\pm 1} &= \left(\omega_{S,\pm 1} \mp \omega_L - v_g \delta k_S \mp \frac{1}{2} D \delta k_S^2\right) \left.\frac{\partial \epsilon}{\partial \omega}\right|_{(k_{S,\pm 1}, \omega_{k_{S,\pm 1}})} \\ &\simeq \pm \left(\delta\omega_S - v_g \delta k_S \mp \frac{1}{2} D \delta k_S^2\right) \epsilon', \end{aligned} \tag{19}$$

having used $\omega_{S,\pm 1} = \delta\omega_S \pm \omega_L$, as well as $\partial\epsilon/\partial\omega|_{(-k_L,-\omega_L)} = -\partial\epsilon/\partial\omega|_{(+k_L,+\omega_L)}$ (ϵ being even with respect to both k and ω), approximated $\partial\epsilon/\partial\omega|_{(k_{S,\pm 1},\omega_{k_{S,\pm 1}})} \simeq \partial\epsilon/\partial\omega|_{(\pm k_L,\pm\omega_L)}$, and finally defined $\epsilon' = \partial\epsilon/\partial\omega|_{(+k_L,+\omega_L)}$.

Then, inserting Eq. (19) into (9) and recalling that $C = \omega_t^2/[(\delta\omega_S - \delta k_S\, v_L)^2 - \omega_B^2]$ gives:

$$-\left(\delta\omega_S - v_g \delta k_S\right)^2 \left(\epsilon'\right)^2 = -\frac{\omega_t^2 D\, \delta k_S^2\, \epsilon'}{(\delta\omega_S - \delta k_S\, v_L)^2 - \omega_B^2}, \tag{20}$$

having neglected the dispersion term D on the left side, but retained it on the right side for being the lowest order contributing term from the expansion for that part of the relation. Equation (20) can be re-written as

$$\left(\delta\omega_S - v_g \delta k_S\right)^2 = \frac{\Gamma^4}{(\delta\omega_S - \delta k_S\, v_L)^2 - \omega_B^2}, \tag{21}$$

where Γ, having units of a frequency, is defined as

$$\Gamma^4 = \frac{\omega_t^2 D\, \delta k_S^2}{\epsilon'}.$$

Considering the fluid-like dielectric function (2), leading to the Bohm-Gross dispersion relation (4) for free EPWs, one obtains:

$$\begin{aligned} \epsilon' &= \left.\frac{\partial \epsilon}{\partial \omega}\right|_{(k_L,\omega_L)} = \frac{2\omega_L}{\omega_{pe}^2}, \\ v_g &= \left.\frac{d\omega}{dk}\right|_{k_L} = 3 v_{\mathrm{th,e}}^2 \frac{k_L}{\omega_L}, \\ D &= \left.\frac{d^2\omega}{dk^2}\right|_{k_L} = 3\lambda_{De}^2 \frac{\omega_{pe}^4}{\omega_L^3}, \end{aligned}$$

so that

$$\Gamma^4 = \frac{3}{2} f_t \left(\delta k_S \lambda_{De}\right)^2 \frac{\omega_{pe}^8}{\omega_L^4}, \tag{22}$$

clearly a positive value.

Equation (21) remains a fourth order polynomial equation for $\delta\omega_S$, still requiring further approximations for obtaining an analytical solution. Let us start by considering relation (21) in the limit of small values of δk_S, $|\delta k_S v_L/\omega_B| \ll 1$. Assuming that the complex frequency $\delta\omega_S \to 0$ as $\delta k_S \to 0$, which can be checked *a posteriori*, one observes that the right side of Eq. (21) reduces to the negative term $-\Gamma^4/\omega_B^2$, clearly providing the condition for an instability, leading to the unstable solution

$$\delta\omega_S = \delta\omega_{S,r} + i\gamma, \quad \text{with} \quad \delta\omega_{S,r} = \mathrm{Re}(\delta\omega_S) = v_g\delta k_S, \quad \text{and} \quad \gamma = \mathrm{Im}(\delta\omega_S) = \frac{\Gamma^2}{\omega_B}. \quad (23)$$

One notices from (23) that $\omega_{S,r}, \gamma \sim \delta k_S$, thus justifying the original assumption that $\delta\omega_S \to 0$ as $\delta k_S \to 0$. The relation $\delta\omega_{S,r} = v_g\delta k_S$ reflects the fact that $\mathrm{Re}(\omega_{S,\pm1})$ is close to the dispersion relation of free EPWs, $\mathrm{Re}(\omega_{S,\pm1}) \simeq \omega_{k_{S,\pm1}}$, as observed in the numerical solution depicted in Fig. 1, indeed:

$$\mathrm{Re}(\omega_{S,\pm1}) = \delta\omega_{S,r} \pm \omega_L \simeq \omega_{k_{S,\pm1}} \simeq \pm\omega_L + v_g\delta k_S \quad \Longrightarrow \quad \delta\omega_{S,r} \simeq v_g\delta k_S,$$

having again used Eq. (18).

To obtain an analytical estimate of the *maximum* growth rate $\gamma_{\max}$, as well as corresponding real frequency $\delta\omega_{r,\max}$ and mode number $\delta k_{\max}$, one makes use of the observation made on the basis of the numerical solutions over a wide range of amplitudes $e\phi_L/T_e$ and wavenumbers $k_L\lambda_{De}$ (see Figs. 3 and 4) that this most unstable mode develops in the vicinity of the resonance $\delta\omega'_{r,\max} = \delta\omega_{r,\max} - \delta k_{\max}v_L = \pm\omega_B$. As the resonance is approached, the right side of Eq. (21) increases, which leads to the maximum growth rate. The resonant condition together with the fact that, even for the most unstable mode, the real frequency still essentially verifies the dispersion of freely propagating EPWs, $\delta\omega_{r,\max} = v_g\delta k_{\max}$, determine a system of two equations for $\delta k_{\max}$ and $\delta\omega_{r,\max}$, yielding:

$$\delta k_{\max} = \mp\frac{\omega_B}{v_L - v_g}, \quad \text{and} \quad \delta\omega_{r,\max} = \mp\omega_B\frac{v_g}{v_L - v_g}. \quad (24)$$

Inserting $\delta\omega_{\max} = \delta\omega_{r,\max} + i\gamma_{\max}$ together with relations (24) into (21) and (22) leads to

$$-\gamma_{\max}^2 = \frac{\Gamma_{\max}^4}{(i\gamma_{\max} \pm \omega_B)^2 - \omega_B^2} \simeq \mp i\frac{\Gamma_{\max}^4}{2\gamma_{\max}\omega_B} \quad \Longrightarrow \quad \gamma_{\max}^3 = \pm i\,\frac{\Gamma_{\max}^4}{2\omega_B},$$

with $\Gamma_{\max}^4 = (3/2)f_t(\omega_B^2\omega_{pe}^6/\omega_L^4)[v_{\mathrm{th,e}}/(v_L - v_g)]^2$ and having assumed $|\gamma_{\max}/\omega_B| \ll 1$. Finally, one obtains

$$\frac{\gamma_{\max}}{\omega_{pe}} = \frac{\sqrt{3}}{2}\left[\frac{3}{4}f_t\,\frac{\omega_B\omega_{pe}^3}{\omega_L^4}\left(\frac{v_{\mathrm{th,e}}}{v_L - v_g}\right)^2\right]^{1/3}, \quad (25)$$

having retained only the maximum real part (as we are mainly interested in the growth rate) among all cubic roots of $\pm i$, *i.e.* $\cos(\pi/6) = \sqrt{3}/2$. Equations (24) and (25) will be compared both to numerical solutions to the KDS dispersion relation as well as to kinetic simulation results in Sec. VI C (see Fig. 16).

V. THE DODIN MODEL

Recently, an improvement to the KDS model has been suggested by Dodin in Ref. [12]. A brief summary of this enhanced model is given here. A systematic derivation starting from the linearized Vlasov-Poisson system, is provided in Appendix B.

In addition to the TPI already described by KDS, the Dodin model includes the Negative Mass Instability (NMI)[12]. The basic mechanism of the NMI is the following: If one considers two trailing trapped particles on a same phase-space orbit, Coulomb repulsion will have these particles switch orbits. The leading particle, which gains energy as a result of the interaction, moves to a less deeply trapped orbit where it sees its bounce frequency decreased, while the trailing particle, losing energy, moves to a more deeply trapped one where it sees its bounce frequency increased. The difference in bounce frequency between the inner and outer orbit leads to the bunching of the particles in their phase-space rotation. This bunching underlies the NMI.

In the Dodin model one essentially makes the same assumptions as for the Kruer model: 1) the Bloch-Floquet -type eigenmodes are reduced to the two dominant Fourier components $\delta\hat{E}_n, n = \pm 1$ (this assumption can however be easily relaxed in both cases), 2) all passing particles are treated as highly passing, 3) trapped particles carry out a harmonic oscillation with amplitude Δx_0 small compared to λ_L, $|k_L \Delta x_0| \ll 1$, which effectively corresponds to a deeply trapped assumption. The essential difference between the Dodin and KDS models is the fact that the former accounts for the decrease of the bounce frequency ω_B between the most deeply trapped particles and the less deeply trapped ones while the later model does not. This variation is clearly a key element in describing the NMI. The actual distribution of trapped particles $f_L(W)$ in the initial LAW, which in general is a function of the particle energy W in the wave frame, must be included. For trapped particles, $W_{\min} < W < W_{\max}$, with $W_{\max\,/\,\min} = \pm e\phi_L$ in case of a sinusoidal wave with amplitude ϕ_L.

The dispersion relation for instabilities in the frame of the Dodin model takes on a very

similar form to the one of KDS [reproducing here Eq. (B23), limited to keeping only $n = \pm 1$, and to be compared to Eq. (10) for KDS]:

$$1 = C_D \left(\frac{1}{\epsilon_{+1}} + \frac{1}{\epsilon_{-1}} \right), \tag{26}$$

with the coupling coefficient C_D taking on the form [repeating Eq. (B21)]:

$$C_D = \omega_t^2 \int_0^{J_{\max}} dJ \, \frac{F(J)}{\omega_B^2 - \delta\omega_S'^2} \left(1 + \frac{2\,\alpha\,\omega_B^2}{\omega_B^2 - \delta\omega_S'^2} \right), \tag{27}$$

having defined the normalized trapped distribution $F(J) = 2\pi f_L(W)/mN_t\lambda_L$, such that $\int_0^{J_{\max}} dJF(J) = 1$, where J is the adiabatic invariant given by the action integral $J = (m/2\pi) \oint v'dx$ over a trapped orbit in the wave frame. Clearly, J is a function of the energy level W. In Eq. (27), the bounce frequency ω_B as well as the coefficient $\alpha = -(J/\omega_B)(d\omega_B/dJ)$, providing a measure of the variation of the bounce frequency between energy levels, are functions of J or equivalently W. Note that in general $\alpha > 0$. Expressing C_D as an integral over J between 0 and $J_{\max} = J(W_c)$ provides its most concise form. However, one can obviously also express C_D as an integral over W between $W_{\min}$ and W_c, as shown in Eq. (B30), and which may be more practical to implement, where W_c is the maximum trapped energy level considered. *A priori*, W_c must be chosen significantly lower than $W_{\max}$ to ensure that the assumption of small oscillation amplitude compared to λ_L is ensured ($|k_L\Delta x_0| \ll 1$).

In the limit of a Dirac distribution, $F(J) = \delta(J - J_0)$, with $J_0 = J(W_0)$ and $W_{\min} < W_0 \ll W_{\max}$, the coupling coefficient C_D reduces to [repeating Eq. (B24)]

$$C_D = C \left(1 - \frac{2\,\alpha_0\,\omega_{B,0}^2}{\delta\omega_S'^2 - \omega_{B,0}^2} \right), \tag{28}$$

with $\omega_{B,0} = \omega_B(W_0)$, $\alpha_0 = \alpha(W_0)$, and C standing for the coupling coefficient (3) appearing in the KDS model. The variation of ω_B and α with respect to W is plotted in Figs. 18.a and 18.c respectively in the case of a sinusoidal wave. Thus, even for the case of a Dirac distribution, the Dodin model accounts for the variation of the bounce frequency $\omega_B(W)$ in the vicinity of $W = W_0$, reflected by the term proportional to α_0 in Eq. (28). Note that if $\alpha_0 = 0$, the Dodin model with Dirac distribution reduces to the Kruer model. As seen from the sinusoidal wave results, Eq. (B29) and corresponding illustration Fig. 18.c., this only takes place for $W_0 = W_{\min}$, *i.e.* considering the limit of the most deeply trapped particles.

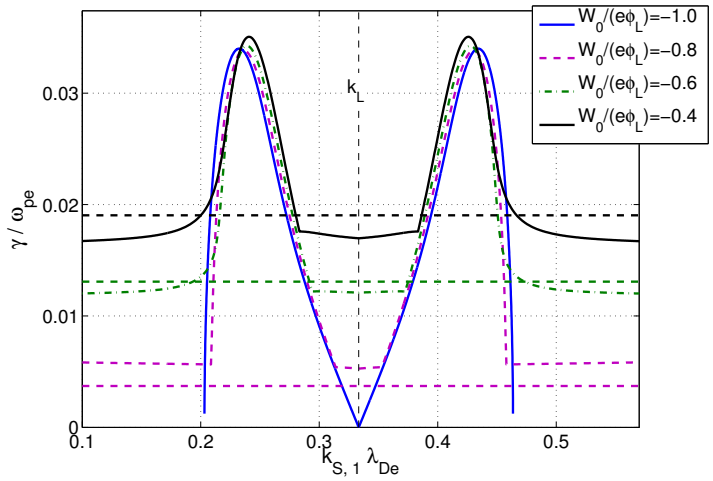

FIG. 5: Solution to the Dodin dispersion relation, assuming a Dirac distribution of trapped particles centered on the energy level W_0. Same parameters for the LAW as in Fig. 1 and again considering (k_L, ω_L) satisfying Bohm-Gross. Shown is the growth rate γ/ω_{pe} of the most unstable mode as a function of the wavenumber $k_{S,1}\lambda_{De}$, for the cases $W_0/(e\phi_L) = -1.0$ (blue), -0.8 (magenta), -0.6 (green), and -0.4 (black). Horizontal dashed lines correspond to the analytical estimates for the NMI growth rate given by Eq. (30) (same color coding for the different values of W_0 as for the numerical solutions).

The dispersion relation (26) together with C_D given by Eq. (28) reduces to a polynomial equation of degree 8. Recall that the KDS dispersion relation is of degree 6. As will be illustrated, the two additional branches of the Dodin model are related to the NMI. Results from this dispersion relation are presented in Fig. 5, considering essentially the same conditions as in Fig. 1, *i.e.* a LAW with wavenumber $k_L\lambda_{De} = 0.333$, frequency $\omega_L/\omega_{pe} = 1.155$ (Bohm-Gross), amplitude $e\phi_L/T_e = 0.5$ and trapped fraction $N_t^{\rm ad}/N = 5.17 \cdot 10^{-3}$ (adiabatic). The energy level W_0 of the Dirac-distributed trapped particles is however set in turn to the different values $W_0/(e\phi_L) = -1.0$, -0.8, -0.6, and -0.4, with the parameters $\omega_{B,0}$ and α_0 evaluated according to Eqs. (B25) and (B29) respectively, providing the values $\omega_{B,0}/\omega_{B,\rm deep} = 1.0$, 0.974, 0.946, 0.917 and $\alpha_0 = 0.0$, $2.71 \cdot 10^{-2}$, $5.91 \cdot 10^{-2}$, $9.78 \cdot 10^{-2}$ respectively. As expected, the result for $W_0/(e\phi_L) = -1.0$ is equivalent to the one obtained with the Kruer model and presented in Fig. 1. Note that in case of a sinusoidal wave one has $k_L\Delta x_0 = \arccos[-W_0/(e\phi_L)]$, providing $k_L\Delta x_0 = 0.00$, 0.64, 0.93, and 1.16 for the

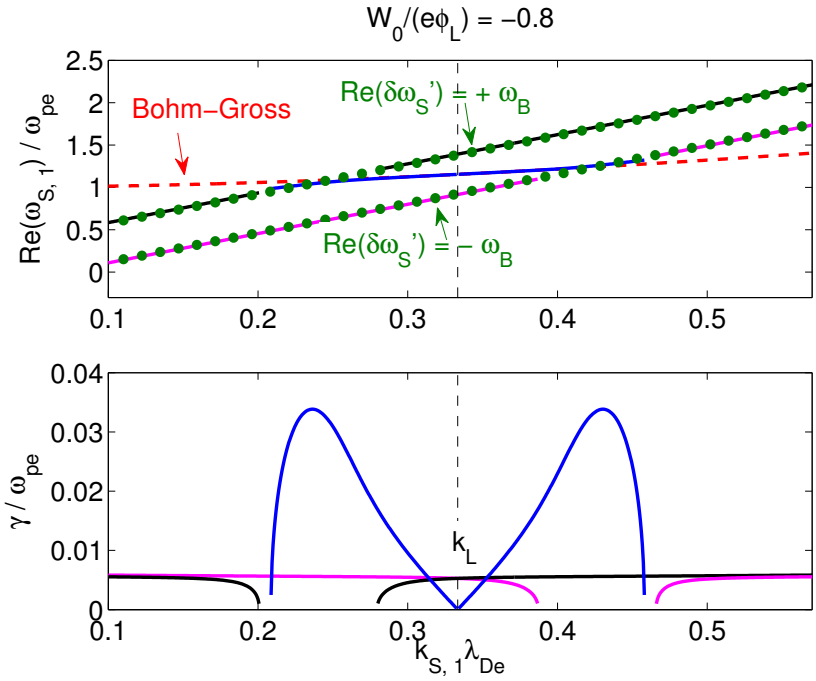

FIG. 6: More detailed spectrum for case $W/(e\phi_L) = -0.8$ of Fig. 5. Shown are both the real frequency $\mathrm{Re}(\omega_{S,1})$ (top plot) and growth rate $\gamma = \mathrm{Im}(\omega_{S,1})$ (bottom) of all unstable roots. One distinguishes the TPI branch (blue line) with real frequency following the Bohm-Gross relation (dashed red), from the NMI branches with real frequency in the wave frame, $\mathrm{Re}(\delta\omega'_S) = \mathrm{Re}(\omega_{S,1}) - k_{S,1}v_L$ equal to either $+\omega_B$ (black) or $-\omega_B$ (magenta).

energy levels $W_0/(e\phi_L) = -1.0$, -0.8, -0.6, and -0.4 respectively. The higher energy levels considered here, $W_0 \gtrsim -0.5$, are thus in fact already beyond the limits of the Dodin model, assuming $|k_L \Delta x_0| \ll 1$.

Figure 5, presenting the growth rate spectrum of the most unstable sideband as a function of $k_{S,1}$, illustrates how the Dodin model clearly still reproduces the TPI branch, which mainly remains unchanged for the different values of W_0 considered. One notices that in the regions of the spectrum where the TPI is not destabilized, an additional instability is clearly visible for $W_0 > -1$, *i.e.* $\alpha_0 > 0$. The situation becomes clearer by plotting all unstable branches, both their real frequency $\mathrm{Re}(\omega_{S,1})$ and growth rate γ, as shown in Fig. 6 for the case $W_0/(e\phi_L) = -0.8$. One notices that in addition to the TPI, with real frequency (in blue) essentially following the Bohm-Gross dispersion relation (dashed red), there is in fact for all $k_{S,1}$ at least one unstable mode (black or magenta) with real frequency in the wave frame

$\mathrm{Re}(\delta\omega'_S) = \mathrm{Re}(\omega_{S,1}) - k_{S,1}v_L$ such that $\mathrm{Re}(\delta\omega'_S) = \pm\omega_B$, characteristic of the NMI [12]. The corresponding growth rates γ are also essentially independent of $k_{S,1}$. The fact that these NMI branches have essentially constant real frequency in the wave frame as well as constant growth rate over the whole k-spectrum reflects that this instability is actually localized in real space. As explained in Ref. [12], the NMI can indeed take place between trapped particles local to a single potential well.

An approximate analytical solution for the NMI can be obtained from the dispersion relation (26) with C_D given by Eq. (28), following a similar derivation as presented in Ref. [12] for the "single trap" case. As illustrated in Fig. 6, the real frequency of the NMI in the wave frame is given by $\mathrm{Re}(\delta\omega'_S) = \mathrm{Re}(\delta\omega_S) - \delta k_S v_L = \mathrm{Re}(\omega_{S,1}) - k_{S,1}v_L \simeq \pm\omega_B$. Except for the wavenumbers δk_S where these two linear curves intersect the Bohm-Gross dispersion relation, the modes $(k_{S,\pm1}, \omega_{S,\pm1})$ are thus non-resonant with the EPW oscillations of the background plasma so that $\epsilon_{\pm1} \simeq 1$ in Eq. (26). One will note from Fig 6 that the NMI branches are indeed only unstable away from the above-mentioned resonances. At the resonance, it is the TPI branch which reaches its largest growth rate, as discussed in Secs. III and IV. For the NMI, one thus approximates the factor appearing in (26) with $(1/\epsilon_{+1} + 1/\epsilon_{-1}) \simeq 2$. Note that this factor should in fact read $\sum_n 1/\epsilon_n$ [see Eq. (B23)], where the sum is taken over all Fourier components n contributing to the instability. For studying the NMI, which contrary to the TPI involves non-resonant Fourier components, the number of these modes should thus in general not be limited to $n = \pm1$ but include all $k_{S,n}$-modes such that $|k_{S,n}\Delta x_0| \lesssim 1$, *i.e.* all Fourier components up to the limit of validity of the Dodin model. For the larger $|k_{S,n}|$ components, the corresponding fluctuation is anyway averaged out over the bounce motion of the trapped particles, leading to much reduced and ultimately zero coupling. For the NMI one therefore should consider the following factor and its approximation:

$$\sum_n \frac{1}{\epsilon_n} \simeq \mathcal{M}, \tag{29}$$

where $\mathcal{M} \simeq 2/(k_L\Delta x_0) \sim \lambda_L/\Delta x_0$. For the parameters considered in Fig. 5, and corresponding estimates for $k_L\Delta x_0$ cited above, one notices that $\mathcal{M}$ will ultimately take on values larger than 2 for the more deeply trapped particle cases.

Combining Eqs. (B23), (28) and (29), one can thus reduce the dispersion relation for the

NMI to

$$1 - \frac{\beta_0}{w}\left(1 - \frac{2\alpha_0}{w}\right) = 0, \quad \Longrightarrow \quad w^2 - \beta_0 w + 2\alpha_0\beta_0 = 0,$$

having defined $\beta_0 = \mathcal{M}\,\omega_t^2/\omega_{B,0}^2$ and $w = (\delta\omega_S'/\omega_{B,0})^2 - 1$. Solving for w provides the two solutions

$$w = \frac{\beta_0 \pm \sqrt{\beta_0^2 - 8\alpha_0\beta_0}}{2},$$

from which one can identify the threshold condition for the NMI: $\alpha_0 > \beta_0/8$. Assuming one is above threshold and that $|w| < 1$ (usually a good approximation), one finally obtains the complex wave frame frequencies for the unstable NMI modes:

$$\begin{aligned}\delta\omega_S' &= \pm\omega_{B,0}\sqrt{1+w} \simeq \pm\omega_{B,0}(1 + w/2) \\ &= \omega_{B,0}\left[\pm\left(1 + \frac{\beta_0}{4}\right) + i\frac{\sqrt{8\alpha_0\beta_0 - \beta_0^2}}{4}\right]. \end{aligned} \tag{30}$$

Note that, as expected, the real frequencies of these two unstable branches are essentially $\pm\omega_B$, with a relative frequency shift $\beta_0/4 \simeq \mathcal{M}f_t/[4(k_L\lambda_{De})^2(e\phi_L/T_e)]$ which is usually very small. For example, $\beta_0/4 \simeq 5\cdot 10^{-2}$ for the case illustrated in Figs 5, considering $\mathcal{M} = 2$, as the Fourier modes were limited to $n = \pm 1$ for obtaining these results. The growth rates estimated with $\gamma = (\omega_{B,0}/4)(8\alpha_0\beta_0 - \beta_0^2)^{1/2}$ according to Eq. (30) are plotted in Fig. 5, showing good agreement with the numerical solutions to the Dodin dispersion relation for the different trapping energy levels considered. One may note that the trapping level $W_0/(e\phi_L) = -0.8$ is in fact very close to the analytical threshold for the NMI as $|\beta_0/(8\alpha_0)| \simeq 0.9$ in this case. The numerical solution to the Dodin dispersion relation indicates stabilization of the NMI for the trapped energy level $W_0/(e\phi_L) \simeq -0.87$ for which $\beta_0/(8\alpha_0) \simeq 1.4$, *i.e.* in relatively good agreement with the analytical estimate.

According to the analytical relation (30), the growth rate for the NMI far above threshold, *i.e.* for $\alpha_0 \gg \beta_0/8$, becomes $\gamma/\omega_{pe} = (\omega_{B,0}/\omega_{pe})(\alpha_0\beta_0/2)^{1/2} = (\mathcal{M}f_t\alpha_0/2)^{1/2}$. In this limit, it is remarkable that the growth rate only depends on the LAW amplitude $e\phi_L/T_e$ through the fraction of trapped particles $f_t = N_t/N$ and not through $\omega_{B,0}$.

VI. KINETIC SIMULATIONS WITH SAPRISTI

A. Simulation model

Kinetic simulations of the non-linear evolution of EPWs were carried out using the SAPRISTI code, which has also been exploited for studying SRS [1], non-linear frequency shifts in both EPWs and (multi-species) IAWs [10, 18], as well as the mechanism of Two Ion Decay (TID) of IAWs and resulting turbulence [19]. The SAPRISTI code considers an Eulerian representation for the distribution of kinetic plasma species in a 1+1-dimensional phase-space (1 configuration space + 1 velocity space dimension). The distributions are evolved according to the Vlasov equation using a semi-Lagrangian advection scheme, which has the advantage of not being limited by a Courant-Friedrichs-Lewy (CFL) stability condition. In turn, the evolution of the self-consistent electromagnetic fields is determined by Maxwell's equations. In the following, the system of equations considered for the simulations presented here are briefly described. More details to the SAPRISTI physical model and its numerical implementation are provided in [9, 10], in particular, Section IIIA of Ref. [10].

For studying the dynamics of sideband instabilities affecting large-amplitude EPWs, a reduced form of the general SAPRISTI model was considered, consisting of the non-linear Vlasov-Poisson system:

$$\left[\frac{\partial}{\partial t} + v\,\frac{\partial}{\partial x} - \frac{e}{m_e}E^{\mathrm{tot}}(x,t)\,\frac{\partial}{\partial v}\right] f_e(x,v,t) = 0, \tag{31}$$

$$-\frac{\partial^2\phi(x,t)}{\partial x^2} = \frac{1}{\epsilon_0}\left[q_i N_i - e\,n_e(x,t)\right]. \tag{32}$$

The Vlasov equation (31) determines the evolution of the electron distribution $f_e(x,v,t)$ in the two-dimensional phase-space (x,v). Ions are assumed immobile, which can be considered a very good approximation for studying the fast time scale dynamics of EPWs. The field $E^{\mathrm{tot}} = E + E^{\mathrm{ext}}$ appearing in (31) represents the total (longitudinal) electrostatic field, superposition of the self-consistent, internal component $E(x,t)$ related to the EPW and of an external component $E^{\mathrm{ext}}(x,t)$ acting as a driver. The internal component $E(x,t) = -\partial\phi/\partial x$ derives from the potential field $\phi(x,t)$, solution to the Poisson equation (32). The charge sources on the right side of Eq. (32) are the uniform, globally neutralizing ion contribution, $q_i N_i$, as well as the fluctuating electron contribution $-e\,n_e(x,t) = -e\int dv f_e(x,v,t)$. Concerning notations, q_i stands for the ion charge, and N_i for the uniform ion density. Global

neutrality reads: $q_i N_i = e\,(1/L)\int_0^L dx\, n_e(x,t)$, where L is the total system length.

For the simulations presented in this paper, the boundary conditions for all physical quantities in the x-direction are periodic. The system is furthermore initialized with a spatially uniform Maxwellian velocity distribution for the electrons: $f_e(x,v,t=0) = f_M(v) = [N/(2\pi v_{\mathrm{th,e}}^2)]\exp[-(1/2)(v/v_{\mathrm{th,e}})^2]$. The large-amplitude EPW is then generated by applying the external driver

$$E^{\mathrm{ext}}(x,t) = E_0^{\mathrm{ext}}(t)\cos(k_L x - \omega^{\mathrm{ext}} t),$$

where k_L is the wavenumber of the LAW one intends to drive and ω^{ext} is chosen in the vicinity of the corresponding wave frequency ω_L, usually estimated from the linear, kinetic dispersion relation (A3). The driver amplitude $E_0^{\mathrm{ext}}(t)$ is smoothly ramped up from essentially zero to a value E_0^{ext} over an initial time interval $0 < t < t_{\mathrm{ramp}}$ of a few wave periods, where it is kept constant until a time $t_{\mathrm{stop}} = t_{\mathrm{ramp}} + t_{\mathrm{drive}}$, after which it is ramped down to zero, again over a time interval of length t_{ramp}. Such a modulation of the external drive allows generation of waves which are freely propagating after the time $t_{\mathrm{stop}} + t_{\mathrm{ramp}}$ and is achieved with a functional form of $E_0^{\mathrm{ext}}(t)$ given by

$$\frac{E_0^{\mathrm{ext}}(t)}{E_0^{\mathrm{ext}}} = \frac{1}{2}\left\{\tanh\left[R\left(\frac{2\,t}{t_{\mathrm{ramp}}} - 1\right)\right] - \tanh\left[R\left(\frac{2\,(t-t_{\mathrm{stop}})}{t_{\mathrm{ramp}}} - 1\right)\right]\right\}. \tag{33}$$

One typically sets $R = 4$ in Eq. (33), ensuring a ramp up (respectively ramp down) of $E_0^{\mathrm{ext}}(t)/E_0^{\mathrm{ext}}$ over the time interval t_{ramp} between ν and $1-\nu$ (respectively $1-\nu$ and ν) with $\nu = 3.4\cdot 10^{-4}$.

For the results presented in this paper, the total simulation length L was chosen between $40\,\lambda_L$ and $100\,\lambda_L$, where $\lambda_L = 2\pi/k_L$ is the wavelength of the LAW one initially drives. Larger systems obviously provide a finer resolution of the spectrum of potentially unstable sideband modes, the resolved Fourier modes having wavenumbers $k = nk_{\mathrm{min}}$, with $k_{\mathrm{min}} = 2\pi/L$ and n taking on integer values up to the Nyquist limit, *i.e.* $|n| \lesssim n_x/2$, n_x being the number of grid points in the x-direction.

B. Simulation example

Results from a typical simulation are summarized in Figures 7 - 15. For this particular case a LAW with wavenumber $k_L\lambda_{De} = 0.333$ was chosen. The wave was generated with an external driver whose frequency ω^{ext} was set to the estimate $\omega_{\mathrm{lin,kin}} = 1.200\,\omega_{pe}$ provided by

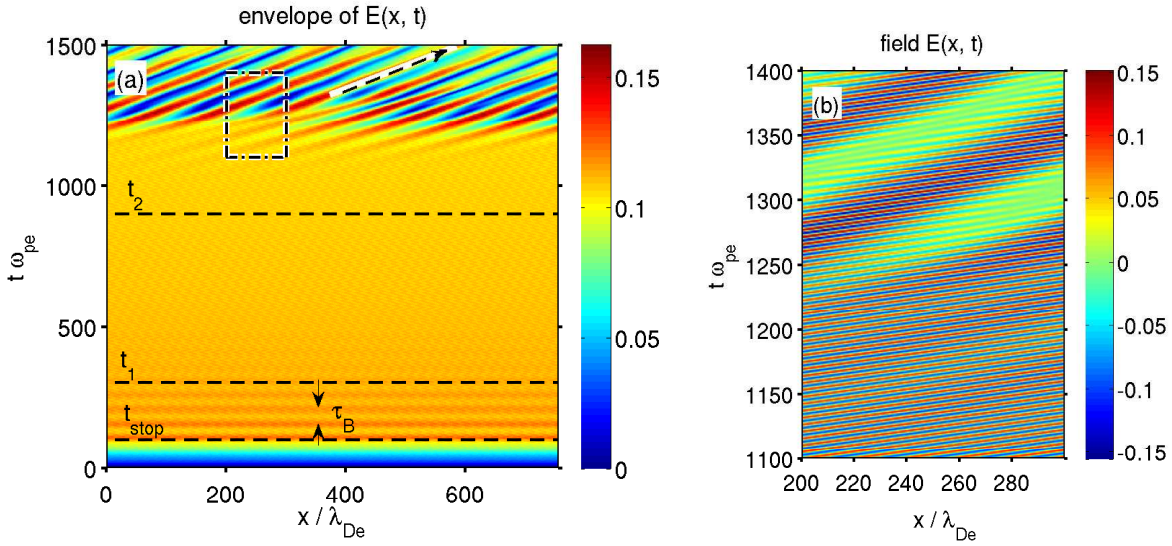

FIG. 7: Time evolution of the internal electrostatic field $E(x,t)$ in units $T_e/e\lambda_{De}$. Plotted is (a) the envelope $|E|$ of the field over the full simulation length and time, as well as (b) a zoom into the limited space and time window $[200,300]\lambda_{De} \times [1100,1400]\omega_{pe}^{-1}$ [corresponding to dashed-dotted delimited region in (a)], showing the full field variation (including fast phase). System length $L = 40\,\lambda_L$ for $k_L\lambda_{De} = 0.333$. External driver is turned off at $t_{\rm stop}\,\omega_{pe} = 100$, at which time the wave amplitude reached $e\phi_L/T_e = 0.33$. The linear growth of sidebands are analyzed in the time interval $t_1 < t < t_2$, with $t_1\omega_{pe} = 300$ and $t_2\omega_{pe} = 900$. The transient modulation in time of the wave envelope shortly after turn-off is related to the bounce period τ_B. The sideband instability enters its fully non-linear stage at $t\omega_{pe} \gtrsim 1200$ at which point the wave-envelope breaks up into wave-packets advecting at the group velocity v_g, estimated from the slope of the dashed arrow as $v_g/v_{\rm th,e} \simeq 1.2$.

the real part of the solution ω to the linear kinetic dispersion relation (A3). The driver had amplitude $E_0^{\rm ext} = 1\cdot 10^{-2}\,T_e/(e\lambda_{De})$ and was turned off at time $t_{\rm stop}\omega_{pe} = 100$ (initial ramp-up and final ramp-down time $t_{\rm ramp}\,\omega_{pe} = 10$), which led to a plasma wave with potential field amplitude $e\phi_L/T_e = 0.33$ (electric field amplitude $e\lambda_{De}E_L/T_e = 0.11$). The system length is 40 wavelengths long, $L = 40\,\lambda_L$, and the numerical resolution in the x-direction was set to $n_x = 2560$ (64 points per wavelength) corresponding to a grid spacing $\Delta x/\lambda_{De} = 0.295$. The maximum of the v_x velocity grid was chosen to be $v_{\rm max} = 8\,v_{\rm th,e}$ and the corresponding number of mesh points $n_v = 512$ providing a spacing $\Delta v/v_{\rm th,e} = 3.125\cdot 10^{-2}$. The time step was set to $dt\,\omega_{pe} = 0.1$.

1. Evolution of wave envelope

The time evolution of the internal electric field envelope $|E|(x,t)$ is shown in Fig. 7.a. The envelope is obtained using a Hilbert transform, as described in [10]. Clearly visible is the progressive increase of the field amplitude up to the time $t_{\rm stop}\,\omega_{pe} = 100$ when the driver is turned off. During a transient period following the plasma wave generation, an oscillation of the field amplitude is observed, whose period can be identified as the bounce period τ_B of trapped particles, estimated from Fig. 7.a as $\tau_B\,\omega_{pe} \simeq 50$. This value can be compared to the theoretical estimate for deeply trapped particles $\tau_{B,\rm deep} = 2\pi/\omega_{B,\rm deep} = 33\,\omega_{pe}^{-1}$, with $\omega_{B,\rm deep}/\omega_{pe} = k_L\lambda_{De}(e\phi_L/T_e)^{1/2}$. The 50% larger period measured in the simulation is related to the fact that the distribution of electrons in the trapping region (see Fig. 14) contains both deeply trapped particles oscillating at the bounce period $\tau_{B,\rm deep}$ as well as marginally trapped ones with bounce period $\tau_B \to \infty$, thus leading to an effective period, averaged over the whole trapping distribution, larger than $\tau_{B,\rm deep}$. The wave envelope clearly starts to break up into wave packets after time $t\,\omega_{pe} \gtrsim 1200$ as a result of a sideband instability. Wave packets advect at the group velocity v_g estimated from Fig. 7.a as $v_g/v_{\rm th,e} \simeq 1.2$, which is in rough agreement (within 30%) with the theoretical estimate using the Bohm-Gross dispersion relation (4): $v_g/v_{\rm th,e} = 3\,v_{\rm th,e}/v_L = 3k_L\lambda_{De}/[1+3(k_L\lambda_{De})^2]^{1/2} = 0.87$ and in excellent agreement with the estimate $v_g = (d/dk){\rm Re}[\omega(k)]|_{k_L} = 1.24\,v_{\rm th,e}$, $\omega(k)$ standing here for the EPW dispersion relation obtained by numerically solving the kinetic dispersion relation (A3). A detailed view of the break-up is provided in Fig. 7.b showing the full field $E(x,t)$ (including its fast phase variation) over the reduced space and time window $[200,300]\lambda_{De} \times [1100,1400]\omega_{pe}^{-1}$.

2. Evolution of sidebands and comparison with KDS model for TPI

The linear evolution of the sideband instability is analyzed by employing a Fourier analysis with respect to the x-direction. The time evolution of the spatial Fourier components $\hat{E}(k)$ of the electric field are shown in Figure 8, where the amplitude $|\hat{E}(k,t)|$ is plotted in logarithmic scale as a function of both wavenumber k and time t. Clearly visible prior to the actual break-up of the wave after $t\,\omega_{pe} \simeq 1200$ is the growth of two lobes of Fourier components on either side of the wavenumber k_L of the LAW, characteristic of the linear development

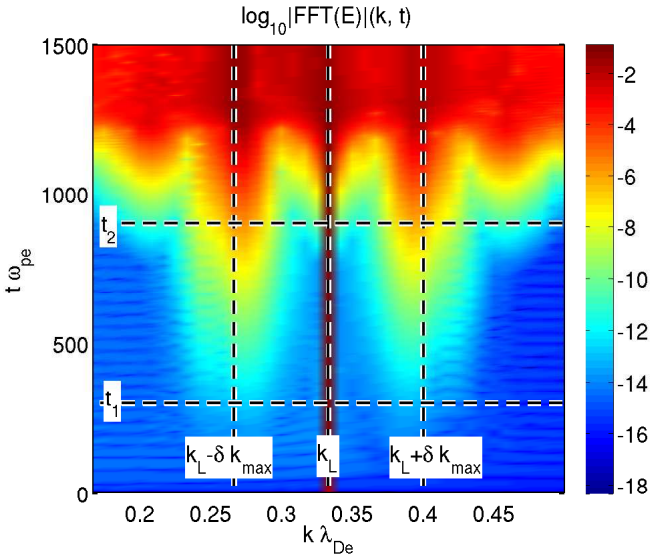

FIG. 8: Same simulation as in Fig. 7. Time evolution of the spatial Fourier spectra $\hat{E}(k,t)$ in the vicinity of the LAW wavenumber $k_L\lambda_{De} = 0.333$. Plotted is $\log_{10}|\hat{E}(k,t)|$. Clearly visible is the development of sideband modes. The linearly most unstable modes involve the Fourier components $k_L \pm \delta k_{\max}$ with $\delta k_{\max}\lambda_{De} = 0.067$. Again pointed out is the time window $[t_1\,\omega_{pe} = 300, t_2\,\omega_{pe} = 900]$ during which the linear evolution of sideband growth is analyzed.

of a sideband instability. The linear evolution of this instability has been further analyzed in the time window $[t_1\,\omega_{pe} = 300, t_2\,\omega_{pe} = 900]$, pointed out in Figs. 7.a, 8, and 9.

The time evolution of a sampling of Fourier component amplitudes $|\hat{E}(k,t)|$ is further detailed in figures 9.a and 9.b in logarithmic and linear scale respectively. The Fourier components shown in Fig. 9.a have wavenumbers $k_L \pm \delta k_S$ with $\delta k_S\lambda_{De} = 0.000, 0.033, 0.067, 0.100$. The components with wavenumbers neighboring k_L clearly present an exponential growth, characteristic of the linear phase of an instability. The growth rate $\gamma(k)$ of each Fourier component is estimated based on an exponential fit $c(k)\exp[\gamma(k)t]$ to its amplitude evolution within the time interval $[t_1, t_2]$. Note how the pairs of modes $k_L \pm \delta k_S$ for each value of $\delta k_S \neq 0$ have essentially equal growth rates in the time window $[t_1, t_2]$. This is in agreement with the presence of Bloch-Floquet type eigenmodes composing the linear phase of the sideband instability. Indeed, as discussed in Sec. II, complex-valued Bloch-Floquet modes are composed of coupled Fourier components with wavenumbers $k_{S,n} = \delta k_S + nk_L$, $|\delta k_S| < k_L/2$, dominant contributions being expected from $n = \pm 1$. Furthermore, as a result

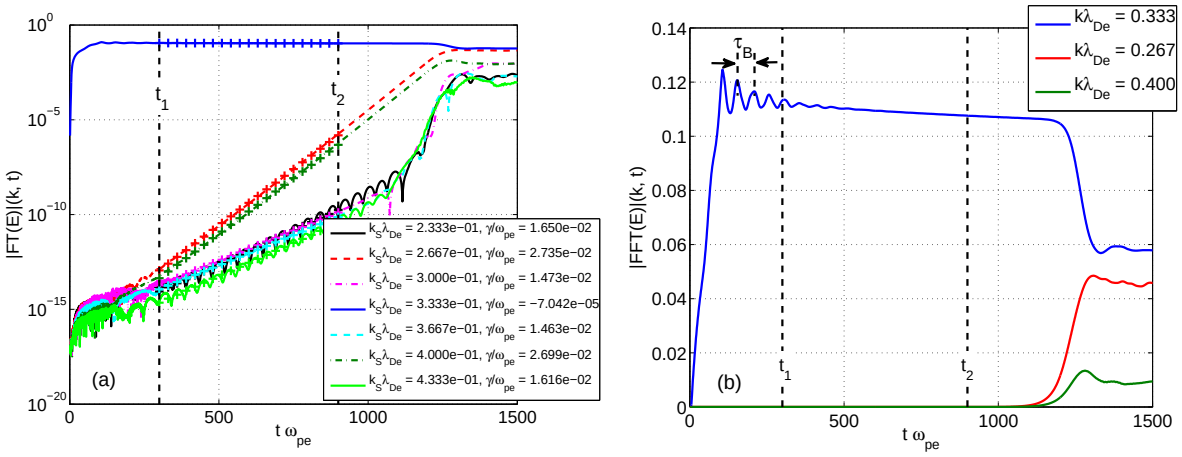

FIG. 9: Same simulation as in Fig. 7. (a) Time evolution in log-lin scale of Fourier component amplitudes for a sampling of wavenumbers $k_L \pm \delta k_S$ with $\delta k_S \lambda_{De} = 0.000, 0.033, 0.067, 0.100$ (corresponding to $\delta k_S / k_{\min} = 0, 4, 8$ and 12 respectively, $k_{\min} = 2\pi/L$). The Fourier components related to the most unstable sideband are for $\delta k_S = \delta k_{\max} = 0.067 \lambda_{De}^{-1}$, *i.e.* $k_L - \delta k_S = 0.267$ and $k_L + \delta k_S = 0.400$. Corresponding growth rate is $\gamma_{\max}/\omega_{pe} = 2.7 \cdot 10^{-2}$. Exponential fits within the time window $[t_1\,\omega_{pe} = 300, t_2\,\omega_{pe} = 900]$ to the evolution of each Fourier component amplitude, from which growth rates are estimated, are shown with crosses. (b) Same but in lin-lin scale and only showing Fourier components k_L and $k_L \pm \delta k_{\max}$, highlighting the relative amplitudes of these modes in the final, non-linearly saturated stage. The Fourier component $k_L - \delta k_{\max} = 0.267$ has the largest sideband amplitude both in the linear and non-linear evolution.

of the reality condition, $E(x,t)$ being a physical field, one has $\hat{E}(-k) = \hat{E}^\star(+k)$, so that in fact the real-valued eigenmode is composed of components $\hat{E}(\pm\delta k_S + n k_L)$, n integer, with $\hat{E}(+\delta k_S + n k_L) = \hat{E}^\star(-\delta k_S - n k_L)$ for each n. Such an eigenmode has a fixed growth rate γ shared by all its Fourier components, in particular the dominant ones, *i.e.* $\hat{E}(\delta k_S + k_L)$ and $\hat{E}(\delta k_S - k_L) = \hat{E}^\star(-\delta k_S + k_L)$.

For the LAW considered here, the most unstable Fourier components are identified for $\delta k_S \lambda_{De} = 0.067$, with a growth rate estimated as $\gamma_{\max}/\omega_{pe} = 2.72 \cdot 10^{-2}$ based on the fit over the time interval $[t_1, t_2]$. The growth rate of all Fourier components with wavenumbers k neighboring k_L are plotted in Fig. 10.a, showing the typical double-humped curve centered around $k = k_L$, as predicted by the KDS model presented in Sec. II. One should indeed note the almost perfect even symmetry around $k = k_L$ of the linear growth rates γ estimated

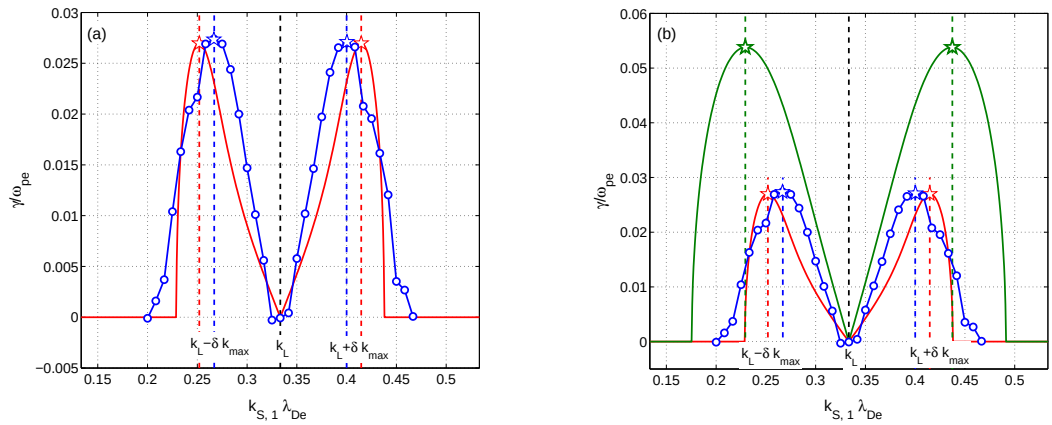

FIG. 10: Same conditions as in Fig. 7. Growth rate $\gamma(k_{S,1})$ of the Fourier component $k_{S,1}$ involved in the linear sideband instability modes. Plotted are results from the simulation (blue) as well as from the KDS model. Maximum growth rate is $\gamma_{\max}/\omega_{pe} = 2.72 \cdot 10^{-2}$ at $\delta k_{\max}\lambda_{De} = 0.067$ for the simulation results (blue stars). (a) Result from the KDS model obtained considering the frequency $\omega_L/\omega_{pe} = 1.15$ of the LAW given by Bohm-Gross (red) and providing the estimate $\gamma_{\max}/\omega_{pe} = 2.70 \cdot 10^{-2}$ at $\delta k_{\max}\lambda_{De} = 0.081$ (red stars). (b) Result from the KDS model considering the frequency $\omega_L/\omega_{pe} = 1.09$ of the LAW as given by the "consistent" non-linear dispersion relation of Eq. (15) (green) leading to $\gamma_{\max}/\omega_{pe} = 5.38 \cdot 10^{-2}$ at $\delta k_{\max}\lambda_{De} = 0.104$ (green stars). Same $\omega_B/\omega_{pe} = 0.191$ and $f_t = 3.13 \cdot 10^{-3}$ was considered as with ω_L from Bohm-Gross.

from the simulation results. Direct comparison to the KDS model is provided by adding to Fig. 10.a the numerical solution to the corresponding dispersion relation (10). For solving the KDS dispersion relation, the frequency of the LAW was first set to the estimate $\omega_L/\omega_{pe} = [1 + 3(k_L\lambda_{De})^2]^{1/2} = 1.15$ provided by the Bohm-Gross dispersion relation (4). The bounce period ω_B and fraction of trapped electrons $f_t = N_t/N$ appearing in the KDS dispersion relation were chosen to be consistent with the amplitude $e\phi_L/T_e = 0.33$ of the LAW considered here. The bounce frequency was thus set to $\omega_B = \omega_{B,\text{deep}} = 0.191\,\omega_{pe}$ and the trapping fraction estimated with the "adiabatic" theoretical relation given by Eq. (A2), providing $f_t = 3.13 \cdot 10^{-3}$ [Eq. (A2) was evaluated with the phase velocity $v_L/v_{\text{th,e}} = 3.464$ given by the Bohm-Gross dispersion relation]. The maximum growth rate predicted by the KDS model in this case is $\gamma_{\max}/\omega_{pe} = 2.70 \cdot 10^{-2}$, *i.e.* within 1% of the maximum growth rate measured in the simulation. This very close agreement needs to be considered as coincidental however, as comparison between simulations and the KDS model over a

wide parameter range of wavenumbers k_L and amplitudes ϕ_L tends to show a more semi-quantitative agreement, as is to be expected given the relative simplicity of the KDS model (this will be further discussed in Sec. VI C in relation with results of Fig. 16). Note already the difference of order 20% in Fig. 10.a between the sideband wavenumber shift $\delta k_{\max}$ of the most unstable Fourier mode measured in the simulation, $\delta k_{\max}\lambda_{De} = 0.067$, and the one, $\delta k_{\max}\lambda_{De} = 0.081$, predicted by the KDS model.

The KDS dispersion relation was then solved considering the estimate $\omega_L/\omega_{pe} = 1.09$ for the LAW frequency provided by the "consistent" non-linear dispersion relation (15), however keeping the values for $\omega_B/\omega_{pe} = 0.191$ and $f_t = 3.13 \cdot 10^{-3}$ unchanged. Corresponding results are shown in Fig. 10.b. The resulting maximum growth rate is $\gamma_{\max}/\omega_{pe} = 5.38 \cdot 10^{-2}$, which is a factor of ~ 2 increase with respect to the maximum sideband growth rate considering ω_L from the (linear) Bohm-Gross dispersion relation. In the same way, the associated $\delta k_{\max}$ is increased by a factor of ~ 1.5 to the value $\delta k_{\max}\lambda_{De} = 0.104$. This significant increase in both $\gamma_{\max}$ and $\delta k_{\max}$ as a result of considering ω_L solution of the non-linear dispersion relation instead of the linear one had already been pointed out in Ref. [16]. While the solution to the KDS model with ω_L from Bohm-Gross is observed to be in good agreement with the simulation results, the strongly modified solution considering ω_L from the non-linear dispersion relation thus significantly differs from the simulations. Consequently, all further estimates with the reduced sideband models, including the derivation of the analytical solution in Sec. IV, were carried out assuming the Bohm-Gross dispersion for ω_L.

Additional evidence that the linear phase of the instability is composed of Bloch-Floquet -type eigenmodes is obtained by further analyzing the set of Fourier components with wavenumber $k_{S,n} = \delta k_S + n k_L$ predicted to form such a mode. Figures 12 and 13 present details of this analysis for the set of Fourier components related to the most unstable sideband $\delta k_S = \delta k_{\max} = 0.067\,\lambda_{De}^{-1}$. Shown in Fig. 12.a is the time evolution of the Fourier amplitude ratios $|\hat{E}(\delta k_{\max} + n k_L)/\hat{E}(\delta k_{\max} - k_L)|$ for $|n| \leq 2$. The component $\hat{E}(\delta k_{\max} - k_L = -0.267\,\lambda_{De}^{-1}) = \hat{E}^{\star}(-\delta k_{\max} + k_L = +0.267\,\lambda_{De}^{-1})$, *i.e.* $n = -1$, has the largest amplitude of the set. In fact, the Fourier component $|k| = 0.267\,\lambda_{De}^{-1}$ has the largest amplitude over all the components composing the sideband throughout the linear *and* non-linear phase of the instability evolution, as already apparent in Figs. 9.a and 9.b. One notes that the amplitude ratios are essentially constant throughout the linear phase $[t_1, t_2]$, which again reflects that, even for this extended set of Fourier components, all elements are simultane-

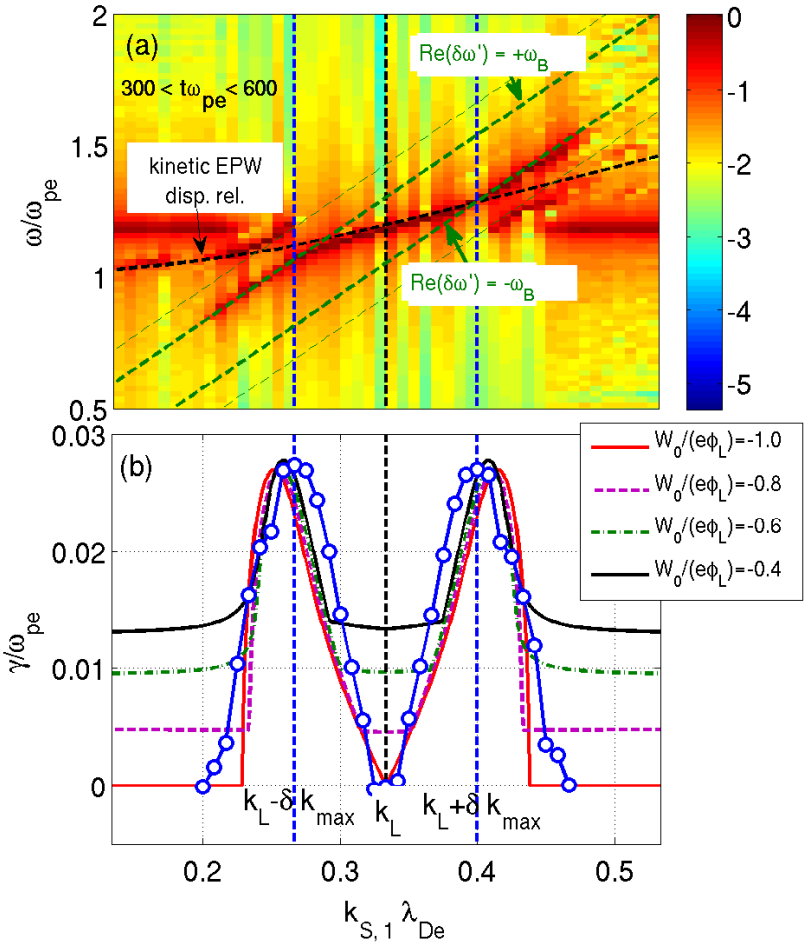

FIG. 11: Same case as in Fig. 10. (a) Amplitude (logarithmic scale) of two-dimensional (k, ω_r)-spectrum of electric field E. Also shown is the solution to the linear kinetic dispersion relation for EPWs (oblique, dashed black line) as well as the condition for resonance in the wave frame with the first (thick green dashed) and second (thin green dashed) harmonic of the bounce frequency ω_B of trapped particles, $\mathrm{Re}(\delta\omega') = \pm\omega_B$ and $\mathrm{Re}(\delta\omega') = \pm 2\omega_B$ respectively. (b) Comparing simulation results with solutions from the Dodin model with Dirac distribution of trapped electrons centered at normalized energy levels $W/(e\phi_L) = -1.0$, -0.8, -0.6, and -0.4. For solving the Dodin model, the frequency $\omega_L/\omega_{pe} = 1.15$ of the LAW given by Bohm-Gross was considered and the fraction of trapped particles was again set to $f_t = 3.13 \cdot 10^{-3}$.

ously increasing with the same growth rate as a result of their coupling. Note however that for $t\,\omega_{pe} \gtrsim 1200$, *i.e.* in the non-linearly saturated phase, the relative amplitudes change significantly. The amplitude ratios averaged over the time window $[t_1'\omega_{pe} = 500, t_2\,\omega_{pe} = 900]$

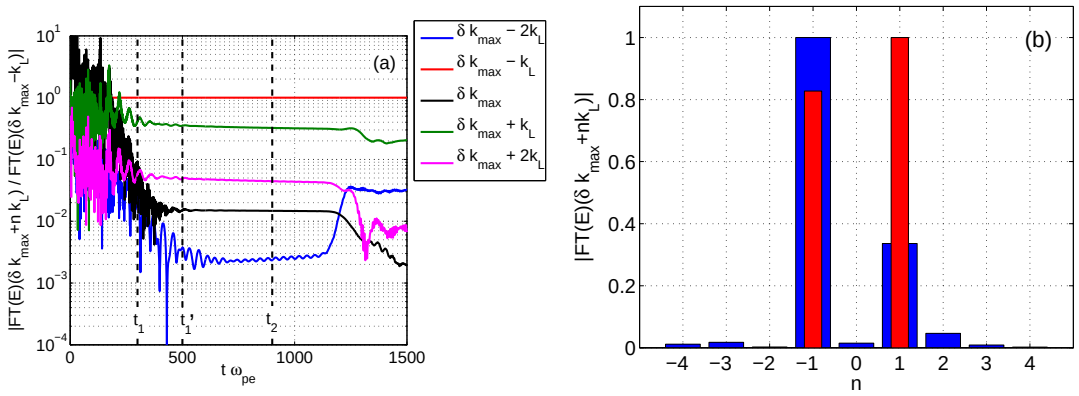

FIG. 12: Same conditions as in Fig. 7. Relative amplitudes of Fourier modes $k_{S,n} = \delta k_{\max} + nk_L$, composing the most unstable Bloch-Floquet -type sideband instability mode. (a) Time evolution of Fourier components from the simulation for $|n| \leq 2$, and $\delta k_{\max}\lambda_{De} = 0.067$. All amplitudes have been normalized to the dominant one, corresponding in this case to $n = -1$. The ratios appear essentially constant in the linear evolution phase delimited by the time window $[t_1\omega_{pe} = 300, t_2\omega_{pe} = 900]$, which reflects that all components have the same common growth rate of the linear eigenmode structure they represent. (b) Relative Fourier mode amplitudes from both the simulation, for $|n| \leq 4$ (blue, time averaged over the window $[t_1'\omega_{pe} = 500, t_2\omega_{pe} = 900]$), and from the KDS model, which considers only $n = \pm 1$ (red, $\delta k_{\max}\lambda_{De} = 0.081$).

in the linear phase are reported for $|n| \leq 4$ in Fig. 12.b. These results clearly validate the assumption made in the KDS model that the dominant Fourier components are $k_{S,n} = \delta k_S \pm k_L$. The next largest Fourier component in the simulation, which is $n = +2$ in this case, indeed only presents a 5% relative amplitude to the largest mode $n = -1$. The relative Fourier amplitudes given by relation (11) for the two components $n = \pm 1$ considered in the KDS model are also shown in Fig. 12.b for the most unstable mode predicted by this model ($\delta k_{\max}\lambda_{De} = 0.081$). Note that the KDS model predicts component $n = +1$ to be dominant instead of $n = -1$ as observed in the simulation.

The instantaneous frequency of each Fourier component can be extracted by taking the time derivative of its phase: $\omega(k,t) = d\,\theta(k,t)/dt$, where $\theta(k,t) = \arg[\hat{E}(k,t)]$ stands for the phase at time t of the Fourier component k. The time evolution of these frequencies for components $k_{S,n} = \delta k_{\max} + nk_L$, $|n| \leq 1$ are shown in Fig. 13.a. Note the equal and constant spacing between these frequencies in the laboratory frame during the linear evolution phase

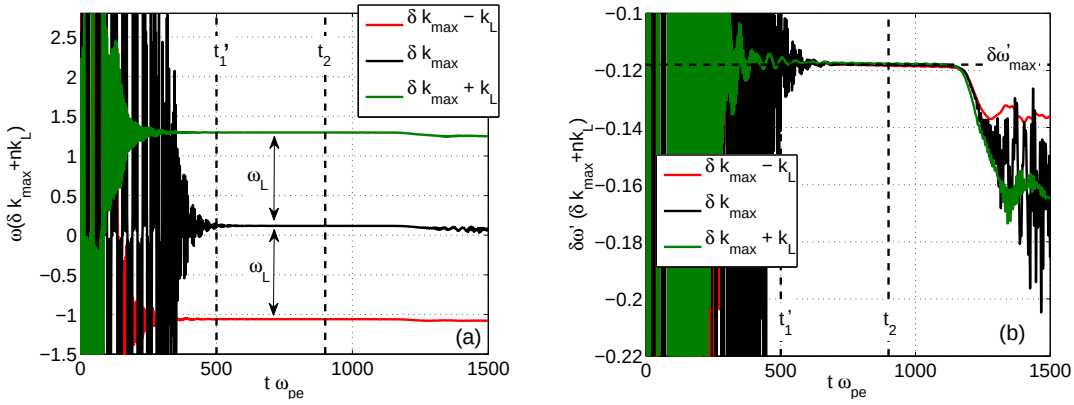

FIG. 13: Same simulation as in Fig. 7. Frequencies of Fourier components $k_{S,n} = \delta k_{\max} + nk_L$ composing the most unstable Bloch-Floquet -type sideband instability mode in both (a) the laboratory frame and (b) the wave frame. Shown are components $|n| \leq 1$. As expected, the frequencies in the wave frame of all Fourier components are equal to a single frequency $\delta\omega'_{\max}$ during the linear stage of the sideband evolution. Note that the frequencies decouple in the non-linear saturated stage, $t\,\omega_{pe} \gtrsim 1200$.

of the instability (the laboratory frame being the one in which the average initial electron velocity is zero). This spacing is identified as the non-linearly (negatively) shifted frequency of the LAW [15, 17], $\omega_{\text{n.l.,sim}}/\omega_{pe} = 1.177$, this value having been directly estimated from the simulation results using the same Hilbert transform -based analysis as presented in [10]. This non-linear frequency is to be compared to the one provided by the linear kinetic dispersion relation for $k_L\lambda_{De} = 0.333$, $\omega_{\text{lin,kin}}/\omega_{pe} = 1.200$. The frequencies in the laboratory frame of the Fourier components $k_{S,n} = \delta k_S + nk_L$ are thus of the form $\omega_{S,n} = \delta\omega_S + n\omega_L$, considering here $\omega_L = \omega_{\text{n.l.,sim}}$, as predicted by theory for a Bloch-Floquet -type eigenmode (see Sec. II). This is further highlighted by Doppler-shifting the frequencies into the wave frame, $\omega' = \omega - kv_L$, $v_L = \omega_{\text{n.l.,sim}}/k_L$ standing here for the non-linear phase velocity of the LAW, leading to the single wave frame frequency $\delta\omega'_S = \delta\omega_S - \delta k_S v_L = \omega_{S,n} - k_{S,n}v_L$ for all Fourier components n, as illustrated in Fig. 13.b. Similar to the amplitudes in Fig. 12.b, the frequencies are significantly modified in the non-linear phase, taking on different values, clearly the sign of a (partial) decoupling of the Fourier components originally composing a linear Bloch-Floquet eigenmode.

3. Comparison with the Dodin model for NMI

The growth rates of unstable Fourier components observed in the simulation results have also been compared to the reduced Dodin model defined by Eqs. (26) and (27). For solving the Dodin model, a Dirac distribution of trapped particles was considered, so that the coefficient C_D coupling the Fourier components is reduced to Eq. (28). The distribution was in turn centered at the normalized energy levels $W_0/(e\phi_L) = -1.0$, -0.8, -0.6, and -0.4, with the bounce frequency $\omega_{B,0}$ and factor α_0 appearing in Eq. (28) taking on corresponding values according to Eqs. (B25) and (B29) respectively. The frequency $\omega_L/\omega_{pe} = 1.15$ of the LAW was estimated from the Bohm-Gross dispersion relation and the fraction of trapped particles $f_t = 3.13 \cdot 10^{-3}$ again consistently set with respect to the amplitude of the LAW. Shown in Fig. 11.b are the most unstable growth rates of each Fourier mode $k_{S,1}$ obtained from the Dodin dispersion relation compared to the simulation results. The solution from the Dodin model for $W_0/(e\phi_L) = -1$ (red curve in Fig. 11.b) is equivalent to the one from the KDS model (also in red in Fig. 10.a) and represents the TPI branch. For all higher energy levels W_0 considered, the NMI branch is clearly present in addition to the TPI, the latter remaining essentially invariant between different values of W_0 while the former presents a growth rate, nearly k-independent, increasing with W_0. These results from the Dodin model are very similar to the ones discussed in detail in Sec. V and presented in Figs. 5 and 6. For all energy levels considered, the growth rate of the NMI is sub-dominant to the maximum value of the TPI branch. Considering ω_L solution to the "consistent" non-linear dispersion relation (B37) instead of the Bohm-Gross estimate again leads to a significant increase of the growth rate of the TPI (the NMI however remains basically unaffected) and is therefore not considered here.

Perhaps the most obvious way to identify the possible presence of a NMI in the simulation results is to analyze the (real) frequency spectrum of the fluctuation field. The NMI is indeed characterized by a real frequency $\delta\omega_r'$ in the wave frame which matches the (average) bounce frequency ω_B of a set of trapped particles and translates in terms of the laboratory frame real frequencies ω_r to the resonant condition $\delta\omega_r' = \omega_r - kv_L = \pm\omega_B$. To resolve eventual multiple frequency components of a same k-mode, a Fourier analysis with respect to time was carried out for each $\hat{E}(k,t)$ instead of the single frequency estimate applied for results in Fig. 13. Furthermore, for the time Fourier analysis of the exponentially growing k-modes

to be relevant, they have beforehand been normalized by corresponding exponential fits $c(k)\exp[\gamma(k)t]$, as the ones shown in Fig. 9. A downside of this normalization procedure is that there is only meaning in comparing the relative amplitude of so-obtained frequency components for a same k-mode but not between different k-modes. The amplitude (in log scale) of the (k, ω_r) spectra of the electrostatic field E from the simulation derived with this approach is plotted in Fig. 11.a. Note that for each unstable Fourier mode k in the interval $[k_L - \delta k_{\max}, k_L + \delta k_{\max}]$ ($\delta k_{\max} = 0.067$ from simulation), the corresponding real frequency spectrum contains mainly a single frequency, which lies very near to the EPW dispersion relation, as predicted by the reduced KDS and Dodin models for the TPI. Here, for the best agreement with simulation results, the real part of the solution to the linear kinetic dispersion relation of EPWs, Eq. (A3), was considered. Near $k = k_L \pm \delta k_{\max}$, one clearly observes in Fig. 11.a that the frequency meets the condition of resonance $\delta\omega_r' = \omega_r - kv_L = \pm\omega_B$ respectively, also in agreement with the prediction for the most unstable sideband mode by the reduced models. The bounce frequency $\omega_B/\omega_{pe} = 0.126$ which was considered for plotting these resonant curves was estimated based on the average bounce period $\tau_B\,\omega_{pe} = 50$ measured in the simulation from Fig. 7, while the phase velocity was estimated as $v_L = \omega_{\text{n.l.,sim}}/k_L = 3.53\,v_{\text{th,e}}$. For $|\delta k| = |k - k_L| \gtrsim \delta k_{\max}$, the real frequency then "sticks" to the relation $\delta\omega_r' \pm \omega_B$, which would be in agreement with the conversion of the most unstable mode from the TPI to the NMI as predicted by the Dodin model and illustrated in Fig. 6. For this same range of k-modes, the frequency spectrum also appears to contain a component resonating with the second harmonic of the bounce frequency, *i.e.* verifying $\delta\omega_r' = \omega_r - kv_L = \pm 2\,\omega_B$, clearly visible in Fig. 11.a. Such resonances with higher order harmonics of the bounce frequency are predicted by the general Goldman theory for sideband instabilities, see Eq. (B12) in Appendix B, but are neglected in the Dodin model. For spatial Fourier modes with $|\delta k| = |k - k_L| \gtrsim 0.12$, there is however no significant exponential growth of sidebands observed in the simulations, contrary to the prediction for the NMI by the simple Dodin model.

4. Distribution of trapped particles

In the framework of the KDS and Dodin models for instabilities affecting LAWs, the dynamics of particles trapped in the initial wave are at the origin of the TPI and NMI

mechanisms. The trapped particle dynamics is in particular characterized in these reduced models by the fraction of trapped electrons $f_t = N/N$ and the bounce frequency ω_B/ω_{pe}. These need to be set consistently when comparing the theoretical predictions of the reduced models with numerical simulation results. It is therefore of interest to take a closer look at the distribution of trapped electrons in phase-space for the EPW simulation discussed here. Assuming that the LAW has essentially reached a stationary state in its own wave frame (BGK-type wave), the distribution of trapped particles is expected to be essentially a function of the particle energy $W = (m/2)v'^2 - e\phi_L(x')$ in the wave frame, $f_{\rm trap} = f_{\rm trap}(W)$, as discussed in more details in Appendix B. This energy distribution of trapped electrons is reconstructed from the simulation following the same procedure as described in [10] and is shown in Figure 14. This numerical result is compared to both limiting theoretical cases "sudden" and "adiabatic" given respectively by Eqs. (9) and (10) in Ref. [10]. Furthermore, for each limiting case, two predictions for the distribution are derived, one assuming a purely sinusoidal field, the other considering the actual numerical field from the simulation. All these theoretical results have been added to Fig. 14. Note that for a given limiting case, "sudden" or "adiabatic", there is little difference whether one assumes a purely sinusoidal field or accounts for the harmonics in the simulation, the latter being very weak for EPWs. Indeed, for the particular case discussed here, the second and third harmonics of the LAW have relative amplitudes $|\delta\hat{E}(2k_L)|/|\delta\hat{E}(k_L)| = 3.4\%$ and $|\delta\hat{E}(3k_L)|/|\delta\hat{E}(k_L)| = 0.2\%$ respectively. The difference between the "sudden" and "adiabatic" distributions are however significant and the trapped electron distribution from the simulation is clearly in much closer agreement with the latter theoretical prediction. This observation validates the choice for estimating the fraction of trapped particles f_t in the reduced models using the "adiabatic" estimate provided by Eq. (A2), which is indeed in very good agreement with the fraction directly estimated from the simulation, as shown in Fig. 17.a. Let us still point out that the "sudden" and "adiabatic" theoretical distributions presented in Fig. 14 assume a fixed phase velocity v_L of the LAW, chosen here as $v_L = \omega_{\rm n.l.,sim}/k_L = 3.531\, v_{\rm th,e}$. More refined estimates for the trapped distribution as presented in Refs. [20] and [21], accounting for the progressive negative non-linear frequency shift of the EPW as its amplitude grows, have therefore been neglected here.

Snapshots of the electron distribution in the (laboratory frame) phase-space (x, v) are shown in Figures 15.a and 15.b. The distribution in Fig. 15.a is for time $t\,\omega_{pe} = 780$, *i.e.* still

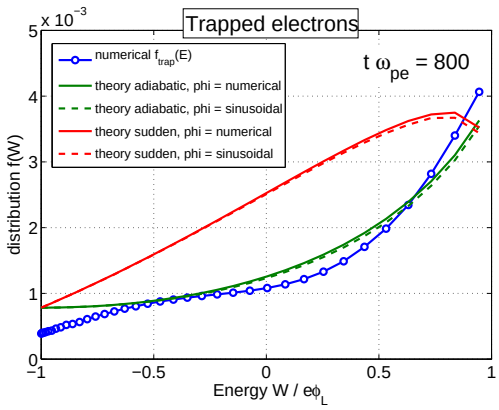

FIG. 14: Same simulation as in Fig. 7. Energy distribution $f(W)$ of trapped electrons from the simulation (blue) at time $t\,\omega_{pe} = 800$, *i.e.* in linear phase of sideband instability evolution. Also shown are the theoretical estimates in both the "adiabatic" (green) and "sudden" (red) limits, considering either the potential field $\phi_L(x)$ provided by the simulation (full lines) or assuming a sinusoidal field with same amplitude (dashed lines).

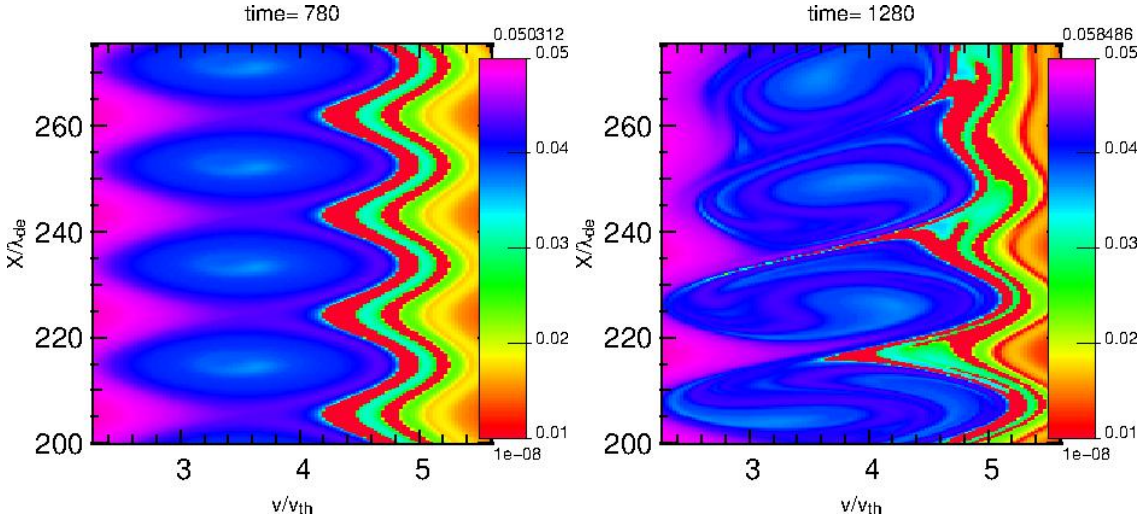

FIG. 15: Phase-space distribution $f(x, v)$ of electrons in the linear stage of the sideband instability evolution at time $t\,\omega_{pe} = 780$ (left) and in the non-linear stage at time $t\,\omega_{pe} = 1280$ (right). Shown is a limited region of the simulation system of the order of 4 wavelengths long in the x-direction and depicting the trapping of particles around the (non-linear) phase velocity $v_L/v_{\mathrm{th,e}} = 3.53$ of the LAW.

in the linear evolution phase of the sideband instability, showing a very coherent state with trapping in the essentially monochromatic initial LAW. The distribution at time $t\omega_{pe} = 1280$

however, shown in Fig. 15.b, is in the non-linearly saturated stage of the sideband instability evolution, clearly showing the presence of a broader fluctuation spectrum.

C. Comparison of simulation results from parameter scan with the KDS model

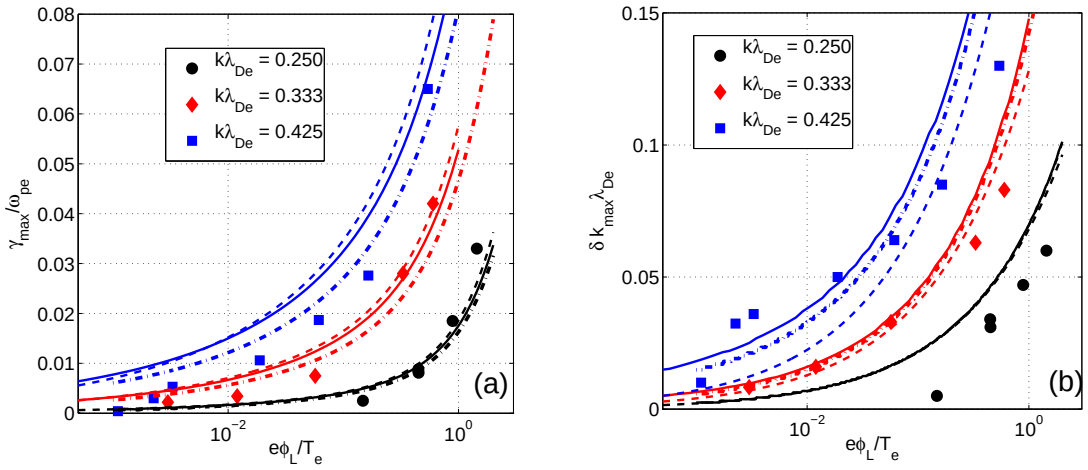

FIG. 16: Comparison of simulation results (markers) with both numerical (full & dash-dotted lines) and analytical (dashed lines) solutions to the KDS dispersion relations. Plotted as a function of the LAW wave amplitude $e\phi_L/T_e$: (a) the normalized growth rate $\gamma_{\max}/\omega_{pe}$ of the most unstable sideband, and (b) the associated quasi-wavenumber $|\delta k_{\max}| = |k_{S,1} - k_L|$. Results shown for $k_L\lambda_{De} = 0.250$ (black), $k_L\lambda_{De} = 0.333$ (red), and $k_L\lambda_{De} = 0.425$ (blue). For the analytical solutions to the KDS model, the fraction of trapped particles f_t was evaluated with v_L estimated from the fluid dispersion relation. For the numerical solutions, f_t was evaluated with v_L from both the fluid (full line) and kinetic (dash-dotted line) dispersion relation.

Simulation results for an extensive parameter scan over both normalized wave amplitude $e\phi_L/T_e$ and wavenumber $k_L\lambda_{De}$ of the initial LAW are summarized in Figure 16. Amplitudes were varied over the range $10^{-3} \lesssim e\phi_L/T_e \lesssim 10^0$ and wavenumbers in turn set to $k_L\lambda_{De} = 0.250$, 0.333, and 0.425. The growth rate $\gamma_{\max}/\omega_{pe}$ of the most unstable sideband is plotted as a function of $e\phi_L/T_e$ for each $k_L\lambda_{De}$ in Fig. 16.a, while the corresponding quasi-wavenumber $\delta k_{\max}$ is reported in Fig. 16.b. Results obtained by numerically solving the KDS dispersion relation (10), as well as the corresponding analytic solution for the most unstable growth rate and associated quasi-wavenumber as given by Eqs. (25) and (24) respectively, are also

shown for comparison.

Both for the numerical and analytical solutions to the KDS model, the frequency ω_L of the LAW was chosen according to the Bohm-Gross dispersion relation, the bounce frequency set to $\omega_B(\phi_L) = \omega_{B,\text{deep}}$ and the fraction of trapped electrons $f_t(\phi_L)$ as given by the "adiabatic" estimate. Concerning this latter parameter, for the analytical solutions to the KDS model the fraction f_t was estimated according to Eq. (A2) using v_L from the fluid dispersion relation (dashed lines in Fig. 16), while for the numerical solutions f_t was estimated using v_L from both the fluid *and* kinetic dispersion relations (full respectively dash-dotted lines in Fig. 16).

One first notes the very good quantitative agreement between the numerical and approximate analytical solutions to the KDS model in all cases (compare corresponding full and dash-dotted lines in Fig. 16), except for $k_L\lambda_{De} = 0.425$ where an increasing relative deviation is observed on $\delta k_{\max}$ between the two results as one goes to lower amplitudes ($\sim 20\%$ and $\sim 60\%$ deviation for amplitudes $e\phi_L/T_e = 10^{-1}$ and 10^{-3} respectively).

The sensitivity of the numerical solutions to the KDS model with respect to how the fraction f_t has been estimated, *i.e.* either using $v_L = v_{L,\text{fluid}}$ from the fluid dispersion relation or $v_L = v_{L,\text{kinetic}}$ from the kinetic dispersion relation, is most pronounced for the highest considered value for the LAW wavenumber, $k_L\lambda_{De} = 0.425$. This is to be expected as the difference between $v_{L,\text{fluid}}$ and $v_{L,\text{kinetic}}$ increases as $k_L\lambda_{De}$ increases. In all cases $v_{L,\text{fluid}} < v_{L,\text{kinetic}}$. Thus for $k_L\lambda_{De} = 0.250$ one has $v_{L,\text{fluid}} = 4.359$ and $v_{L,\text{kinetic}} = 4.424$, representing a difference of less than 2%, while for $k_L\lambda_{De} = 0.425$ one has $v_{L,\text{fluid}} = 2.922$ and $v_{L,\text{kinetic}} = 3.101$, representing a difference of 6%. The *larger* kinetic estimate for v_L leads to a *reduced* trapped fraction f_t (see Fig. 17.a), as a result of the number of particles decreasing as one goes further out in the tail of the velocity distribution. Finally, due to the fact that the fraction of trapped particles f_t represents the drive to the sideband instabilities, as clearly illustrated by Eq. (25), a reduction in f_t leads to a reduced growth rate γ of the sidebands. This is reflected in Fig. 16.a by the dash-dotted lines lying systematically below the full lines, the deviation being almost imperceptible for $k_L\lambda_{De} = 0.250$ however more significant ($\sim 15\%$) for $k_L\lambda_{De} = 0.425$.

Given the relative simplicity of the KDS model, the quantitative agreement between the results from this reduced model and the simulations is remarkably good, especially for the higher amplitudes $e\phi_L/T_e$ of the LAW (less than 10% difference on $\gamma_{\max}$ in almost all cases

for $e\phi_L/T_e \gtrsim 3 \cdot 10^{-1}$). At lower amplitudes, and especially for the largest wavenumber considered, $k_L\lambda_{De} = 0.425$, the agreement becomes more semi-quantitative on both the growth rate $\gamma_{\max}$ and the wavenumber $\delta k_{\max}$. One may nonetheless note in Fig. 16.a that the agreement for lower amplitudes $e\phi_L/T_e$ in the cases $k_L\lambda_{De} = 0.333$ and $k_L\lambda_{De} = 0.425$ between the simulations and the KDS model is somewhat better when the fraction of trapped particles f_t for these latter results has been estimated using $v_{L,\text{kinetic}}$ instead of $v_{L,\text{fluid}}$, consistent with the fact that the estimate for f_t using $v_{L,\text{kinetic}}$ is expected to be more accurate. At higher amplitudes the simulation results for $\gamma_{\max}$ tend to show closer agreement with the KDS results using f_t estimated with $v_{L,\text{fluid}}$. One might interpret this effect as resulting from a *negative* non-linear frequency shift of the large-amplitude EPWs, which becomes especially important for higher values of $e\phi_L/T_e$ and $k_L\lambda_{De}$, having the tendency of shifting v_L from the linear kinetic estimate $v_{L,\text{kinetic}}$ down towards the fluid estimate $v_{L,\text{fluid}}$ [10].

For all cases however, the KDS model appears to correctly capture the main dependence of the most unstable longitudinal sideband of EPWs with respect to the basic parameters $k_L\lambda_{De}$ and $e\phi_L/T_e$ characterizing the initial LAW, in particular increased growth rate $\gamma_{\max}$ and wavenumber $\delta k_{\max}$ when either increasing $k_L\lambda_{De}$ or $e\phi_L/T_e$. This most unstable sideband observed in the simulations can therefore be clearly identified of TPI nature.

VII. CONCLUSIONS

Using the Vlasov-Poisson code SAPRISTI, we carried out a series of non-linear kinetic simulations to address the stability of large-amplitude EPWs to longitudinal sideband instabilities in a spatially one-dimensional, periodic system.

Detailed analysis of the initial, linear evolution phase of the instabilities affecting the LAWs confirmed the presence of Bloch-Floquet type eigenmodes as predicted by the general linear stability theory of periodic waves by Goldman [13]. In particular, it was shown that the spatial Fourier components $k_{S,n} = \delta k_S + nk_L$, $|\delta k_S| < k_L/2$, composing the eigenmodes all have the same growth rate $\gamma(\delta k_S)$ and real frequency $\delta\omega'_S(\delta k_S)$ in the wave frame. Together with the reality condition, this leads to γ being a perfectly even function with respect to δk_S, which has also been verified in the simulation results.

Simulation results were also compared to numerical solutions to the sideband dispersion relation provided by the relatively simple reduced model derived by Kruer, Dawson and

Sudan (KDS) [8] for the Trapped Particle Instability (TPI) as well as to the more general dispersion relation proposed by Dodin [12], a variant of the KDS model that accounts for the Negative Mass Instability (NMI). Both these reduced models were systematically derived from the general Goldman theory which allowed their numerous approximations to be pointed out clearly.

Comparing the growth rate $\gamma_{\max}$ and corresponding quasi-wavenumber $\delta k_{\max}$ of the most unstable sideband mode in the simulations to the KDS model over scans of the wavenumber (range $0.250 < k_L\lambda_{De} < 0.425$) and amplitudes (range $10^{-3} \lesssim e\phi_L/T_e \lesssim 10^0$) of the initial EPW has shown good agreement at high amplitudes and low wavenumbers and at least semi-quantitative agreement for the lower amplitudes and higher wavenumbers. The most unstable sideband was thus identified to have a TPI character. A practical approximate analytical solution to the KDS dispersion relation for this most unstable mode was therefore derived and shown to be in good agreement with the numerical solution. The detailed analysis of the most unstable sideband in the simulations furthermore showed that this mode is essentially composed of the two dominant Fourier component $k_{S,\pm1}$, with wavenumber-frequency pairs close to the dispersion relation of freely propagating EPWs, thus providing further validation for one of the essential assumptions made in the reduced models for the TPI.

In fact, the real frequency spectrum of unstable sidebands in the simulations shows that for $|\delta k_S| \leq |\delta k_{\max}|$ the frequency of the dominant spatial Fourier components composing the sideband follows the dispersion relation for EPWs, as predicted by the reduced models for the TPI, while for $|\delta k_S| > |\delta k_{\max}|$ the real (wave frame) frequency follows the condition of resonance with the bounce frequency of trapped particles, which is a feature characteristic of the NMI according to the Dodin model. Despite this indication of the possible presence of NMI in the simulations, a dedicated study will need to be carried out to confirm whether this instability mechanism is indeed at play. This shall be the topic of a following paper.

The primary practical motivation for the analysis carried out in this paper was to investigate the role of the TPI in the saturation of SRS. The TPI growth rates shown in Fig. 16 are significant over a wide range of wave numbers $k_L\lambda_{De}$ and larger, for similar parameters, than the growth rates of LDI which may also affect the EPW driven by SRS. Indeed, neglecting damping of the IAW and daughter EPW in the LDI dispersion relation given by Eq. (51)

in Ref. [7], one finds the LDI growth rate:

$$\gamma_{LDI} = \frac{1}{4}\sqrt{\frac{Zm_e}{m_i}}\frac{\omega_L^2}{\sqrt{\omega_a\omega_L}}\frac{k_a}{k_L}\frac{(k_L\lambda_{De})^2}{1+(k_a\lambda_{De})^2}\frac{e\phi_L}{T_e},$$

where $k_a \simeq 2k_L$ and $\omega_a \simeq k_a c_s$ stand for the wavenumber and frequency of the IAW involved in the LDI mechanism, $c_s = (ZT_e/m_i)^{1/2}$ being the sound velocity, Z the ionization degree and m_i the ion mass. One thus obtains the estimate:

$$\frac{\gamma_{LDI}}{\sqrt{\omega_a\omega_L}} \sim \frac{1}{4}\frac{k_L\lambda_{De}}{1+4(k_L\lambda_{De})^2}\frac{e\phi_L}{T_e}, \tag{34}$$

which, for $k_L\lambda_{De} = 0.333$, yields $\gamma_{LDI}/\sqrt{\omega_a\omega_L} \sim 6\cdot 10^{-2}\, e\phi_L/T_e$. For ease of comparison to TPI growth rates and for the parameters just given and $Zm_e/m_i = 1/1836$, note that $\gamma_{LDI}/\omega_{pe} \sim 7\cdot 10^{-3}\, e\phi_L/T_e$, which is significantly smaller than the TPI growth rates shown in Fig. 16 for the same value of $k_L\lambda_{De}$. Setting the LDI threshold by the condition that $\gamma_{LDI}^{\rm thresh} = \sqrt{\nu_i\nu_e}$, where ν_i and ν_e are the damping rates of the daughter IAW and EPW respectively, and making use of Eq. (34), one finds the amplitude threshold on the initial EPW:

$$\frac{e\phi_L^{thresh}}{T_e} \sim 4\frac{1+4(k_L\lambda_{De})^2}{k_L\lambda_{De}}\sqrt{\frac{\nu_i}{\omega_a}\frac{\nu_e}{\omega_{pe}}}.$$

Considering again $k_L\lambda_{De} = 0.333$ and the Landau damping rate estimates $\nu_i/\omega_a \gtrsim 0.1$ and $\nu_e/\omega_{pe} = 0.02$, as appropriate for a CH or Helium plasma with $T_i/T_e = 0.5$, often used in Inertial Fusion experiments, one obtains $e\phi^{\rm thresh}/T_e \sim 0.8$. According to our simulations, this threshold is clearly much larger than any threshold for growth of the TPI. No threshold for the TPI was in fact observed in our simulations, even at the lowest amplitudes considered.

We have also simulated with a 2D+2V Vlasov code [22] the transverse sideband (filamentation) instability in systems one wavelength long in the propagation direction, such that this longitudinal TPI is precluded [23]. In that case, the growth rates are similar but no larger than found for the longitudinal TPI, even for high values of $k\lambda_{De}$.

VIII. ACKNOWLEDGMENTS

We are pleased to acknowledge very valuable discussions with J. W. Banks, T. Chapman, I. Dodin, W. Rozmus, and L. Yin. This work was performed under the auspices of the U.S. Department of Energy by Lawrence Livermore National Laboratory under Contract DE-AC52-07NA27344 and funded by the Laboratory Research and Development Program at LLNL under project tracking code 12-ERD-061.

Appendix A: Estimating the fraction of trapped particles

For evaluating the parameter ω_t appearing in relation (3) for the coupling coefficient C of the KDS dispersion relation (10), one must estimate the average density N_t of particles trapped in the LAW. To lowest order in the wave amplitude one expects $N_t \sim \Delta v_t f_0(v_L)$, where $f_0(v)$ stands for the initial electron distribution, typically assumed Maxwellian, and $\Delta v_t = 2\sqrt{e\phi_L/m}$ for the trapping width in velocity space. The resulting scaling for the fraction of trapped particles, $f_t = N_t/N \sim (e\phi_L/T)^{1/2}$, however already breaks down at very low wave amplitudes and a more accurate estimate for f_t must be found. Here and in the following, the subscript 'e', identifying electron-specific quantities, is dropped with the intent of lightening notations.

The fraction of trapped particles f_t not only depends on the amplitude ϕ_L, but also on how the LAW was generated. The two limiting cases of "sudden" and "adiabatic" generation [15], both leading to a BGK-type waves [14], have been considered, providing two different estimates for $f_t = N_t/N$. Assuming an initial Maxwellian electron distribution, $f_0 = f_M = [N/(2\pi v_{\mathrm{th,e}}^2)] \exp[-(1/2)(v/v_{\mathrm{th,e}})^2]$ and a sinusoidal wave field, the "sudden" generation provides the fraction:

$$\frac{N_t^{\mathrm{sud}}}{N} = \frac{1}{2\lambda_L} \int_{-\lambda_L/2}^{+\lambda_L/2} dx \left[\mathrm{erf}\left(\frac{v_L + \Delta v_t \cos(k_L x/2)}{\sqrt{2} v_{\mathrm{th,e}}} \right) - \mathrm{erf}\left(\frac{v_L - \Delta v_t \cos(k_L x/2)}{\sqrt{2} v_{\mathrm{th,e}}} \right) \right], \tag{A1}$$

while the "adiabatic" generation gives

$$\frac{N_t^{\mathrm{ad}}}{N} = \frac{1}{2} \left[\mathrm{erf}\left(\frac{v_L + 2\Delta v_t/\pi}{\sqrt{2} v_{\mathrm{th,e}}} \right) - \mathrm{erf}\left(\frac{v_L - 2\Delta v_t/\pi}{\sqrt{2} v_{\mathrm{th,e}}} \right) \right]. \tag{A2}$$

In Eqs. (A1) and (A2), $\lambda_L = 2\pi/k_L$ stands for the wavelength of the LAW and $\Delta v_t/v_{\mathrm{th,e}} = 2\sqrt{e\phi_L/T_e}$ for the trapping width in velocity space. More details to the derivation of these equations are provided in Sec. IV.D of Ref. [10]. It should be pointed out that, in obtaining relations (A1) and (A2), the phase velocity v_L of the wave is approximated to remain fixed. Accounting for the progressive negative non-linear frequency shift of the EPW as its amplitude grows, leading to an associated progressive down-shift of v_L, which may clearly affect the estimate of the fraction f_t, has therefore been neglected. This effect has been accounted for in more advanced trapping models developed by Bénisti and Gremillet [20] as well as by Lindbergh [21]. However, given the many approximations intrinsic to the reduced KDS and Dodin models considered in this paper, such a refined estimate for f_t is not considered here.

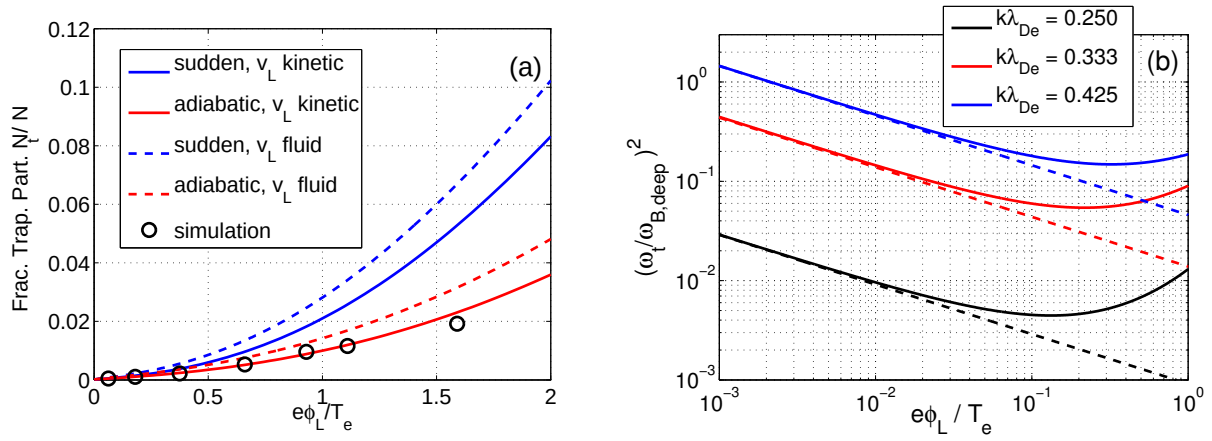

FIG. 17: (a) Sudden (blue) and adiabatic (red) estimates for the fraction of trapped particles f_t as a function of normalized wave amplitude $e\phi_L/T_e$ for EPWs with $k_L\lambda_{De} = 0.333$. The fraction f_t was estimated using either the fluid (dashed lines) or the kinetic (full lines) dispersion relation for evaluating the phase velocity v_L of the LAW. Comparison with simulation results (black circles). (b) Ratio $(\omega_t/\omega_{B,\mathrm{deep}})^2 = f_t/[(k_L\lambda_{De})^2 e\phi_L/T_e]$ as a function of wave amplitude, using the adiabatic estimate for f_t with v_L from the kinetic dispersion relation (full lines) and considering cases $k_L\lambda_{De} = 0.250$ (black), 0.333 (red), and 0.425 (blue). Same cases but considering the lowest order estimate $f_t \simeq (4/\pi)\Delta v_t\, f_0(v_L)/N$ (see Eqs. (67) and (69) Ref.[10]) and leading to $(\omega_t/\omega_{B,\mathrm{deep}})^2 \sim (e\phi_L/T_e)^{-1/2}$ are plotted with dashed lines.

Results from relations (A1) and (A2) for the fractions of trapped particles are shown in Figure 17.a as a function of normalized wave amplitude $e\phi_L/T_e$ for EPWs with $k_L\lambda_{De} = 0.333$ and compared with simulation results for sufficiently slowly driven waves, consequently showing good agreement with the adiabatic theoretical estimate. Note that the phase velocity $v_L = \omega_L/k_L$ of the LAW is required for evaluating (A1) and (A2). Two estimates for v_L were considered here, obtained by either making use of the *fluid* (Bohm-Gross) dispersion relation (4) or numerically solving the *kinetic* linear dispersion relation for EPWs, given by

$$\epsilon(k,\omega) = 1 + \frac{1}{(k\lambda_{De})^2}\mathcal{W}\left(\frac{\omega}{kv_{\mathrm{th,e}}}\right) = 0, \tag{A3}$$

where ϵ stands here for the kinetic dielectric function [instead of the fluid relation (2)] and using the notation $\mathcal{W}(z)$ for the Maxwellian dispersion function defined as:

$$\mathcal{W}(z) = \frac{1}{\sqrt{2\pi}}\int_\Gamma \frac{x}{x-z}\exp(-x^2/2)dx, \tag{A4}$$

Γ standing for the Landau contour. For $k_L\lambda_{De} = 0.333$, the complex solution to (A3) gives $\omega/\omega_{pe} = 1.200 - i\,2.59 \cdot 10^{-2}$, and thus $\tilde{v}_L = \omega_L/(k_L v_{\rm th}) = 3.600$, having considered $\omega_L = {\rm Re}(\omega)$. Figure 17.a clearly illustrates that the best agreement with the simulation results is obtained with the adiabatic estimate for the trapped fraction using v_L based on the linear kinetic dispersion relation.

Appendix B: Fully kinetic and reduced models for sideband instabilities

The main purpose of this appendix is to show how the different reduced models (KDS and Dodin) considered in this paper for the sideband instability can be derived from Goldman's exact kinetic theory for the stability of large periodic plasma waves [13], thereby clearly pointing out the different approximations underlying the reduced models.

1. The Goldman theory

The fully kinetic framework for studying sideband instabilities affecting a LAW is given by the Vlasov-Poisson system (31)-(32), recalled here in the form:

$$\left[\frac{\partial}{\partial t} + v\,\frac{\partial}{\partial x} + \frac{e}{m}\frac{\partial \phi(x,t)}{\partial x}\,\frac{\partial}{\partial v}\right] f(x,v,t) = 0, \tag{B1}$$

$$-\frac{\partial^2 \phi(x,t)}{\partial x^2} = \frac{1}{\epsilon_0}\left[q_i N_i - e\int dv f(x,v,t)\right]. \tag{B2}$$

In the following, the free evolution of waves is addressed, so that the electric field E acting on the electrons has been reduced in Eq. (B1) to the internal contribution $E = -\partial\phi/\partial x$. Note that, as in Appendix A, the subscript 'e', identifying electron-specific quantities, is dropped.

One assumes initially a finite-amplitude BGK-type wave, which must be represented in its own wave-frame by a stationary solution $[f_L(x',v'), \phi_L(x')]$ to the system (B1)-(B2), *i.e.* verifying:

$$\left[v'\,\frac{\partial}{\partial x'} + \frac{e}{m}\frac{d\phi_L(x')}{dx'}\,\frac{\partial}{\partial v'}\right] f_L(x',v') = 0, \tag{B3}$$

$$-\frac{d^2\phi_L(x')}{dx^2} = \frac{1}{\epsilon_0}\left[q_i N_i - e\int dv' f_L(x',v')\right], \tag{B4}$$

where $x' = x - v_L t$ and $v' = v - v_L$ are respectively the position and velocity in the wave frame, v_L being the phase velocity of the LAW in the laboratory frame. The general

solution $f_L(x', v')$ to (B3) is given by any function of the constants of motion: particle energy $W = (m/2)v'^2 - e\phi_L(x')$ and in addition, for untrapped particles only, the sign $\sigma = \text{sign}(v')$ of velocity. Inserting such a function $f_L(W, \sigma)$ into Eq. (B4) leads to an effective non-linear differential equation for $\phi_L(x)$, which in general admits periodic solutions, representing a wave train. The corresponding period λ_L is identified as the wavelength of the LAW and one defines the associated fundamental wavenumber $k_L = 2\pi/\lambda_L$ and laboratory frequency $\omega_L = k_L v_L$. How to conveniently solve the effective equation for ϕ_L is discussed in the original paper [14] on BGK waves by Bernstein, Greene, and Kruskal.

To carry out a stability analysis of the LAW, one considers small-amplitude perturbations $[\delta f(x', v', t), \delta\phi(x', t)]$ of the stationary solution $[f_L(x', v'), \phi_L(x')]$ and linearizes the system (B1)-(B2), leading to

$$\left[\frac{\partial}{\partial t} + v'\,\frac{\partial}{\partial x'} + \frac{e}{m}\frac{d\phi_L(x')}{dx'}\,\frac{\partial}{\partial v'}\right]\delta f(x', v', t) = -e\frac{\partial\delta\phi(x', t)}{\partial x'}v'\frac{\partial f_L(W, \sigma)}{\partial W}, \tag{B5}$$

$$\frac{\partial^2\delta\phi(x', t)}{\partial x'^2} = \frac{e}{\epsilon_0}\int dv'\delta f(x', v', t). \tag{B6}$$

Equation (B5) can be solved for δf in terms of $\delta\phi$ by integrating along the unperturbed trajectories, corresponding to the evolution of electrons in the potential field ϕ_L. This can at least be done formally, but in practice may require numerical integration. Inserting the so-obtained perturbed distribution δf into (B6) finally leads to an effective linear equation for $\delta\phi$ or, alternatively, for the associated perturbed electric field $\delta E = -\partial\delta\phi/\partial x$. This has been formally carried out by Goldman in Ref. [13] for a general λ_L-periodic stationary state (f_L, ϕ_L), in which case the linear solutions describing the sidebands are of Bloch-Floquet -type. For example, the electric field perturbation $\delta E = -\partial\delta\phi/\partial x$ reads in the wave frame:

$$\delta E(x', t) = \exp\left[i(\delta k_S x' - \delta\omega'_S t)\right]\sum_{n=-\infty}^{+\infty}\delta\hat{E}_n\exp(ink_L x'). \tag{B7}$$

Characteristic of a Bloch-Floquet mode representing a perturbation in a λ_L-periodic system, note in (B7) the single frequency $\delta\omega'_S$ in the wave frame and the spatial dependence given by the product of a λ_L-periodic function, $\sum_n \delta\hat{E}_n\exp(ink_L x')$, and a plane wave, $\exp(i\delta k_S x')$, where δk_S is referred to as the quasi- wavenumber and can always be chosen within the first Brillouin zone ($|\delta k_S/k_L| < 1$). In the laboratory frame, the Bloch mode (B7) becomes

$$\delta E(x, t) = \sum_{n=-\infty}^{+\infty}\delta\hat{E}_n\exp\left[i(k_{S,n}x - \omega_{S,n}t)\right], \tag{B8}$$

with $k_{S,n} = \delta k_S + n k_L$, $\omega_{S,n} = \delta\omega_S + n\omega_L$, and $\delta\omega_S = \delta\omega'_S + \delta k_S v_L$. Contrary to (B7), relation (B8) is the superposition of Fourier modes with different frequencies separated by harmonics $n\omega_L$.

Let us summarize here the effective, linear equation obtained for the sidebands by carrying out the Goldman approach. One in fact obtains a system of equations coupling the different Fourier coefficients $\delta\hat{E}_n$ appearing in Eq. (B7), which can be written in the form:

$$\sum_{n'=-\infty}^{+\infty} \boldsymbol{\epsilon}_{n,n'}(\delta k_S, \delta\omega'_S)\, \delta\hat{E}_{n'} = 0, \quad \forall n, \tag{B9}$$

with the dielectric coupling matrix elements given by:

$$\boldsymbol{\epsilon}_{n,n'}(\delta k_S, \delta\omega'_S) = \delta_{n,n'} + \chi_{n,n'}(\delta k_S, \delta\omega'_S), \tag{B10}$$

$\delta_{n,n'}$ standing for the Kronecker symbol and $\chi_{n,n'}$ appearing as the electric susceptibility coupling matrix elements. These elements have both a contribution $\chi^t_{n,n'}$ and $\chi^u_{n,n'}$ from trapped and untrapped (passing) electrons respectively:

$$\chi_{n,n'} = \chi^t_{n,n'} + \chi^u_{n,n'} = -\frac{e^2}{m\epsilon_0\lambda_L k_{S,n} k_{S,n'}} \left(I^t_{n,n'} + I^u_{n,n'}\right), \tag{B11}$$

with

$$I^{\mathrm{t}}_{n,n'} = \int_{W_{\min}}^{W_{\max}} dW\, \frac{d\, f_L(W)}{dW}\, \tau_0 \sum_{p=1}^{+\infty} \frac{2(p\,2\pi/\tau_0)^2}{(p\,2\pi/\tau_0)^2 - \delta\omega'^2_S}\, C^\star_p(k_{S,n}, W)\, C_p(k_{S,n'}, W), \tag{B12}$$

$$I^{\mathrm{u}}_{n,n'} = \sum_{\sigma=\pm 1} \int_{W_{\max}}^{+\infty} dW\, \frac{\partial f_L(W,\sigma)}{\partial W}\, \tau_0 \times \sum_{p=-\infty}^{+\infty} \frac{p\,2\pi/\tau_0 + k_{S,n'}\langle v'\rangle_\tau}{p\,2\pi/\tau_0 + k_{S,n'}\langle v'\rangle_\tau - \delta\omega'_S}\, C^\star_{p+\sigma(n'-n)}(k_{S,n}, W, \sigma)\, C_p(k_{S,n'}, W, \sigma), \tag{B13}$$

$W_{\min} = -e\max_x(\phi_L)$ and $W_{\max} = -e\min_x(\phi_L)$ standing respectively for the minimum and maximum energy levels of trapped electrons. The complex coefficients C_p ($C^\star_p$ stands for the complex conjugate of C_p) appearing in Eqs. (B12)-(B13) are in fact Fourier coefficients with respect to time of the phase factor

$$\exp\left\{ik\left[x'(\tau) - \langle v'\rangle_\tau \tau\right]\right\} = \sum_{p=-\infty}^{+\infty} C_p(k, W(,\sigma))\, \exp(ip\frac{2\pi}{\tau_0}\tau), \tag{B14}$$

where $x'(\tau)$ is the unperturbed trajectory, function of time τ, corresponding to the energy level W and with initial condition $x'(\tau = 0) = x'_0$, x'_0 being chosen as either one of the

turning points for trapped particles and as $x'_0 = 0$ (resp. $x'_0 = \lambda_L$) for forward (resp. backward) passing particles, *i.e.* with $\sigma = +1$ (resp. $\sigma = -1$). Having defined the time-averaged velocity $\langle v' \rangle_\tau$, with $\langle v' \rangle_\tau = 0$ for trapped particles and $\langle v' \rangle_\tau = \sigma \lambda_L / \tau_0$ for passing, subtracting the average trajectory $\langle v' \rangle_\tau \tau$ from $x'(\tau)$ in the phase factor on the left side of Eq. (B14) ensures that one indeed has a time-periodic function for which the Fourier series is well defined. This period τ_0 is clearly equal to the bounce period τ_B for trapped particles and to the transit time (=time required to cross one wavelength λ_L) for passing particles. Note that C_p is a function of (k, W) for trapped particles and (k, W, σ) for passing. All the information related to the unperturbed trajectories and relevant to the linear response of the system is thus reduced to the quantities τ_0, $\langle v' \rangle_\tau$ and C_p. The denominators in Eqs. (B12)-(B13) obviously represent possible resonances between the wave frequency (Doppler-shifted for passing particles) and p-harmonics of the bounce/transit frequencies of particles.

For fixed quasi- wavenumber δk_S, (B9) thus defines an eigenvalue equation, with eigenfrequency $\delta \omega'_S$ and corresponding eigenvector given by the set of Fourier coefficients $\{\delta \hat{E}_n\}_n$. This is obviously a non-standard eigenvalue equation, as the matrix elements $\boldsymbol{\epsilon}_{n,n'}$ are intricate (non simply linear) functions of $\delta \omega'_S$. The associated dispersion relation, relating $\delta \omega'_S$ to δk_S is given by

$$\det \left[\boldsymbol{\epsilon}(\delta k_S, \delta \omega'_S) \right] = 0,$$

where $\boldsymbol{\epsilon}$ is the matrix with elements $\boldsymbol{\epsilon}_{n,n'}$. The eigenvalue system defined by Eqs. (B9)-(B13) is similar to the one presented in Ref. [13] [see Eqs. (18), (19), (36)-(39) therein] but given here in a more symmetric form, which was essentially achieved by transforming the spatial integrals in Eqs. (37) and (39) of Ref. [13] by time integrals, this change of variable being defined by the particle trajectories $x' = x'(\tau)$.

2. The reduced KDS and Dodin models

In both the KDS and Dodin models, the passing electrons are all approximated as highly passing, *i.e.* essentially unaffected by the presence of the LAW and therefore carrying out trajectories with uniform velocity v': $x'(\tau) = x'_0 + v'\tau$. As $\langle v' \rangle_\tau = v'$ in this case, the phase factor on the left side of Eq. (B14) becomes a simple constant $\exp(ikx'_0)$, and the only non-zero coefficient C_p is $C_0 = \exp(ikx'_0)$. As a result, the sum in Eq. (B13) is reduced to the zeroth order transit frequency harmonic, $p = 0$, and furthermore, as expected, the

contribution to $\chi_{n,n'}$ from untrapped particles is only non-zero for $n = n'$, reflecting that there is no Fourier mode coupling from these highly passing particles. Finally, $\tau_0 = \lambda_L/|v'|$ in this limit, so that Eq. (B13) becomes

$$\begin{aligned} I^{\mathrm{u}}_{n,n'} &\simeq \delta_{n,n'} \sum_{\sigma=\pm 1} \int_{W_{\max}}^{+\infty} dW \, \frac{\partial f_L}{\partial W} \, \frac{\lambda_L}{|v'|} \, \frac{k_{S,n} v'}{k_{S,n} v' - \delta\omega'_S} \simeq \delta_{n,n'} \lambda_L \int dv' \frac{\partial f_L/\partial v'}{v' - \delta\omega'_S/k_{S,n}} \\ &= \delta_{n,n'} \lambda_L \int dv \frac{\partial f_L/\partial v}{v - \omega_{S,n}/k_{S,n}} \simeq -\delta_{n,n'} \frac{N\lambda_L}{v_{\mathrm{th}}^2} \frac{1}{\sqrt{2\pi}} \int d\mathsf{v} \frac{\mathsf{v} \exp(-\mathsf{v}^2/2)}{\mathsf{v} - \omega_{S,n}/(|k_{S,n}| v_{\mathrm{th}})} \\ &= -\delta_{n,n'} \frac{N\lambda_L}{v_{\mathrm{th}}^2} \mathcal{W}\left(\frac{\omega_{S,n}}{|k_{S,n}| v_{\mathrm{th}}} \right), \end{aligned} \tag{B15}$$

having changed variables from the wave frame energy W to the wave frame velocity v' and finally to the laboratory frame velocity $v = v_L + v'$, as well as invoked $\omega_{S,n} = \delta\omega'_S + k_{S,n} v_L$. Furthermore, f_L has been approximated by the original Maxwellian f_M, thus neglecting the deformation of the distribution by the LAW, which is consistent with the highly passing approximation. Finally, integration is carried out over the whole velocity space, thus assuming that the trapped fraction is small ($f_t \ll 1$). The function $\mathcal{W}(z)$ stands for the Maxwellian dispersion function given by Eq. (A4). By inserting Eq. (B15) into Eq. (B11), one then obtains the following highly passing electron contribution to the electric susceptibility coupling matrix:

$$\chi^u_{n,n'} \simeq \delta_{n,n'} \frac{1}{(k_{S,n}\lambda_D)^2} \mathcal{W}\left(\frac{\omega_{S,n}}{|k_{S,n}| v_{\mathrm{th}}} \right). \tag{B16}$$

For the trapped particles as well, the same approximations are made in both the KDS and Dodin model for computing the corresponding coefficients C_p. Indeed, the trapped particles are all assumed to carry out a trajectory which is harmonic: $x'(\tau) = x'_{\min} + \Delta x_0 \cos(\omega_B \tau)$, where $x'_{\min}$ is the location in the wave frame of the bottom of the potential well felt by the electrons. This is obviously an approximation except in the true limit of deeply trapped particles. What shall distinguish the Dodin from the KDS model is that the former accounts for the variation of the bounce frequency ω_B with respect to the different possible trapped energy levels $W_{\min} < W < W_{\max}$ [ω_B clearly decreases with respect to W, with $\omega_B(W_{\min}) = \omega_{B,\mathrm{deep}} > 0$ and $\omega_B(W_{\max}) = 0$], while the latter model neglects this variation. The amplitude of oscillation Δx_0 is furthermore assumed small compared to all wavelengths considered,

$|k\Delta x_0| \ll 1$, so that Eq. (B14) becomes (recall $\langle v' \rangle_\tau = 0$ for trapped particles):

$$\begin{aligned}
\exp[ikx'(\tau)] &= \exp(ikx'_{\min}) \exp\left[ik\Delta x_0 \cos(\omega_B \tau)\right] \\
&\simeq \exp(ikx'_{\min}) \left[1 + ik\Delta x_0 \cos(\omega_B \tau)\right] \\
&= \sum_{p=-\infty}^{+\infty} C_p \exp(ip\,\omega_B \tau),
\end{aligned}$$

having Taylor expanded to first order the exponential with argument $\sim k\Delta x_0$, so that $C_p \simeq 0$ for all p except $C_0 = \exp(ikx'_{\min})$ and $C_{\pm 1} = \exp(ikx'_{\min})\, ik\Delta x_0/2$. According to (B12), C_0 does not contribute to the trapped particle response. Furthermore, note that, without loss of generality, the origin of the coordinate system can always be shifted such that $x'_{\min} = 0$, which shall be considered here (let us point out that this same assumption is also implicit in the original derivation of the KDS model in Ref. [8]). Inserting these relations for C_p into Eq. (B12) leads to

$$\begin{aligned}
I^{\mathrm{t}}_{n,n'} &= \frac{k_{S,n} k_{S,n'}}{2} \int_{W_{\min}}^{W_{\max}} dW\, 2\pi \frac{d\, f_L(W)}{dW} \;\; \frac{\omega_B \Delta x_0^2}{\omega_B^2 - \delta\omega_S'^2} \\
&= \frac{k_{S,n} k_{S,n'}}{m} \int_0^{J_{\max}} dJ\, 2\pi \frac{d\, f_L(J)}{dJ} \;\; \frac{J}{\omega_B^2 - \delta\omega_S'^2},
\end{aligned} \tag{B17}$$

having used $\omega_B\, \tau_0 = 2\pi$ and changed variables from energy W to the adiabatic invariant J given by the action integral

$$J = (m/2\pi) \oint v' dx,$$

the integral being carried out over a full trapped orbit and thus estimating the enclosed surface in phase-space. One has the relation $J = (m\lambda_L/\pi)\bar{u}'$, where

$$\bar{u}'(W) = \langle u'(x, W) H(W + e\phi_L) \rangle_x,$$

stands for the spatially averaged velocity of a particle with energy W, $u' = [(2/m)(W + e\phi_L(x))]^{1/2}$, $\langle A \rangle_x = (1/\lambda_L) \int_{-\lambda_L/2}^{+\lambda_L/2} A$ for the spatial average of quantity A over one wavelength, and H for the Heaviside function. One makes use here of the notation J for the sole purpose of considering the same definitions and recovering the same relations as in Ref. [12]. For a particle carrying out an essentially harmonic trajectory, one in particular has $J = m\omega_B \Delta x_0^2/2$, which has been invoked in the last step leading to relation (B17). The notation $J_{\max} = J(W_{\max})$ is used for the maximum value of J, reached by the

marginally trapped particles. Finally, by combining Eqs. (B11) and (B17), the following trapped electron contribution to the electric susceptibility coupling matrix is derived:

$$\chi^t_{n,n'} = -\frac{N_t e^2}{m\epsilon_0}\int_0^{J_{\max}} dJ\,\frac{d\,(2\pi f_L/mN_t\lambda_L)}{dJ}\;\frac{J}{\omega_B^2-\delta\omega_S'^2}$$
$$= -\omega_t^2\int_0^{J_{\max}} dJ\,\frac{d\,F(J)}{dJ}\;\frac{J}{\omega_B^2-\delta\omega_S'^2}, \tag{B18}$$

having made use of the relation $\omega_t^2 = N_t e^2/(m_e\epsilon_0)$ and defined $F(J) = 2\pi f_L/mN_t\lambda_L$. As the density of trapped particles is given by

$$N_t = \frac{1}{\lambda_L}\int_{\rm trap} dx'dv' f_L(x',v') = \int_{W_{\min}}^{W_{\max}}\frac{dW}{m}\langle\frac{H(W+e\phi_L)}{u'(x,W)}\rangle_x\sum_{\sigma=\pm1} f_L(W,\sigma) \tag{B19}$$

$$= \int_0^{\bar{u}'(W_{\max})} d\bar{u}'\,2\,f_L = \frac{2\pi}{m\lambda_L}\int_0^{J_{\max}} dJ f_L, \tag{B20}$$

having made use of $d\bar{u}'/dW = (1/m)\langle H(W+e\phi_L)/u'(x,W)\rangle_x$ and $\sum_{\sigma=\pm1} f_L(W,\sigma) = 2f_L(W)$ for trapped particles, one can deduce that F verifies the normalization $\int_0^{J_{\max}} dJF(J) = 1$.

Note that relation (B18) for $\chi^t_{n,n'}$ is independent of n, n' and thus provides the same coupling between all pairs of Fourier components $(k_{S,n}, k_{S,n'})$ in the Bloch-Floquet -type eigenmode solution (B7). One should emphasize that in deriving Eq. (B18) the assumption of low-amplitude harmonic trajectories was in fact only invoked for deriving the coefficient C_p appearing in the numerator of the integrant to the J-integral, while no assumption was made in deriving what one may expect to be the more sensitive resonant denominator. Nonetheless, the low-amplitude assumption, $|k\Delta x_0| \ll 1$ invalidates relation (B18) for all but the more deeply trapped particles, even though, as discussed in Sec. II, only the Fourier modes with the lower wavenumbers $k_{S,n=\pm1}$ significantly contribute to and therefore need to be considered in estimating the Bloch-Floquet modes (at least for the TPI). Indeed, even for these wavenumbers one has $|k_{S,n=\pm1}\Delta x_0| \simeq 2\pi\Delta x_0/\lambda_L > 1$ for marginally trapped particles, as they have an oscillation amplitude approaching $\Delta x_0 = \lambda_L/2$. In practice one is thus led to consider distributions $F(J)$ that go to zero clearly below $J_{\max}$. For practical purposes, it is convenient to transform relation (B18) using integration by parts and invoking $F(J_{\max}) = 0$, which leads to

$$\chi^t_{n,n'} = \omega_t^2\int_0^{J_{\max}} dJ\,\frac{F(J)}{\omega_B^2-\delta\omega_S'^2}\left(1+\frac{2\,\alpha\,\omega_B^2}{\omega_B^2-\delta\omega_S'^2}\right), \tag{B21}$$

having defined $\alpha = -(J/\omega_B)(d\omega_B/dJ)$.

The general form of the reduced Dodin model is obtained by combining relations (B16) and (B18) into (B9)-(B11), leading to the eigenvalue equation:

$$\epsilon_n \, \delta\hat{E}_n = C_D \sum_{n'=-\infty}^{+\infty} \delta\hat{E}_{n'}, \quad \forall n, \tag{B22}$$

with $\epsilon_n = \epsilon(k_{S,n}, \omega_{S,n})$ and $\epsilon(k,\omega)$ the dielectric function for an homogeneous plasma given by Eq. (A3), usually approximated in the fluid limit by Eq. (2), and the "Dodin" coupling coefficient $C_D = -\chi^t_{n,n'}$ with $\chi^t_{n,n'}$ given by Eq. (B18) [or equivalently (B21)]. Dividing Eq. (B22) by ϵ_n and summing over all n leads to

$$\left(1 - C_D \sum_{n=-\infty}^{+\infty} \frac{1}{\epsilon_n}\right) \sum_{n=-\infty}^{+\infty} \delta\hat{E}_n = 0,$$

from which one derives the dispersion relation

$$1 = C_D \sum_{n=-\infty}^{+\infty} \frac{1}{\epsilon_n}. \tag{B23}$$

When limiting the Fourier modes to $n = \pm 1$, the eigenvalue equation (B22) takes on essentially the same form as the system (7)-(8) and the corresponding dispersion relation (B23) the same form as (10) (with C replaced by C_D). Note that Eq. (B23) is identical to Eq. (5) in Ref. [12].

The simplest form of the Dodin model is to consider all trapped particles as being localized at a single energy level $W = W_0$ with corresponding action integral $J_0 = J(W_0)$, so that the distribution of trapped particles reads $F(J) = \delta(J - J_0)$, where $\delta(x)$ stands for the Dirac distribution. This particular form of the distribution indeed verifies the required normalization $\int dJ\, F = 1$. From Eq. (B21) one then obtains:

$$C_D = \frac{\omega_t^2}{\delta\omega_S'^2 - \omega_{B,0}^2}\left(1 - \frac{2\,\alpha_0\,\omega_{B,0}^2}{\delta\omega_S'^2 - \omega_{B,0}^2}\right) = C\left(1 - \frac{2\,\alpha_0\,\omega_{B,0}^2}{\delta\omega_S'^2 - \omega_{B,0}^2}\right), \tag{B24}$$

with $\omega_{B,0} = \omega_B(W_0)$, $\alpha_0 = \alpha(W_0)$, and C standing for the coupling coefficient (3) appearing in the KDS model. Notice from (B24) that in case of $\alpha_0 = 0$ one has $C_D = C$ and the Dodin model reduces to the KDS model. KDS thus appears as a particular case of Dodin in which all trapped particles are located at a same energy level $W = W_0$ and with the additional assumption of $\alpha_0 = -(J/\omega_B)(d\omega_B/dJ)|_{W_0} = 0$. This assumption is however only correct at the very bottom of the potential well, *i.e.* for $W_0 = W_{\min}$, where $J_0 = 0$. For any other

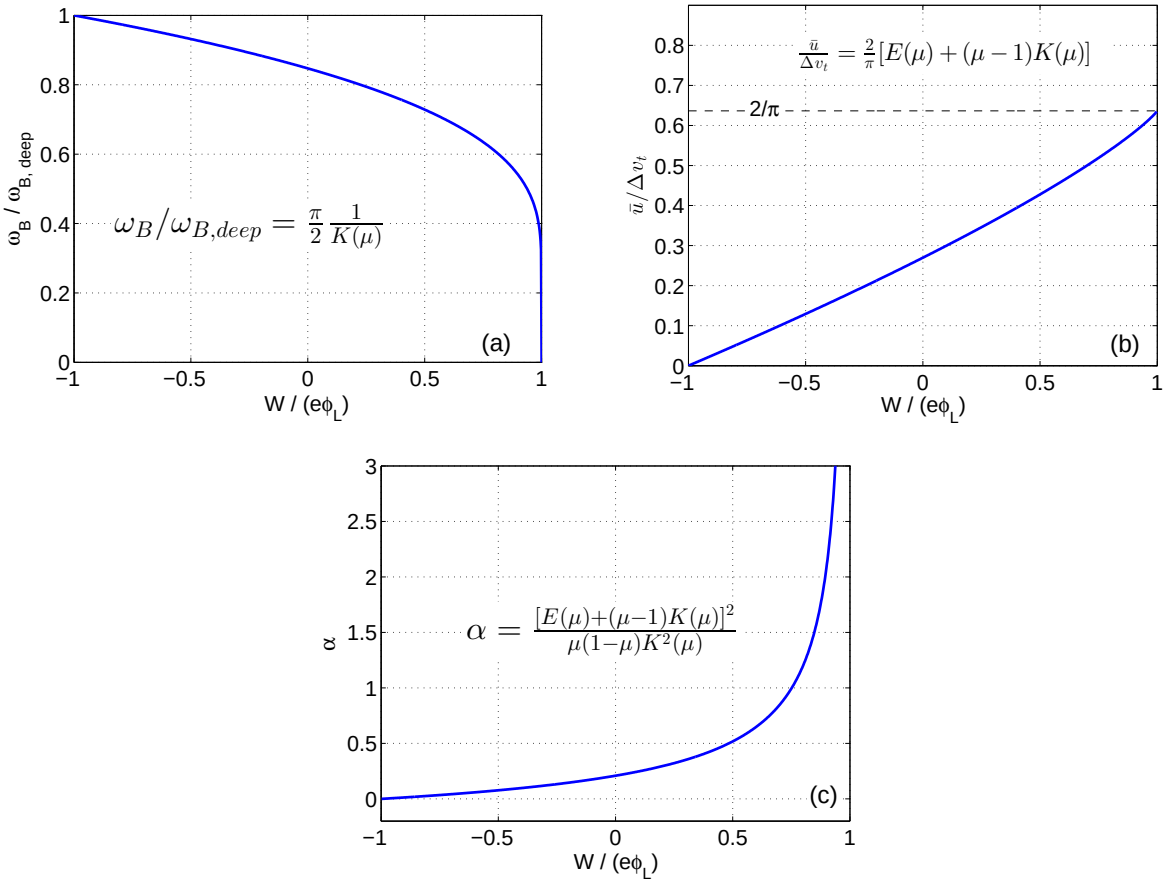

FIG. 18: (a) Bounce frequency ω_B, (b) x-averaged velocity $\bar{u}' = (\pi/m\lambda_L)J$, and (c) $\alpha = -(J/\omega_B)(d\omega_B/dJ)$ as a function of energy level W for particles trapped in a sinusoidal field.

trapped energy level, $W_{\min} < W_0 \leq W_{\max}$, α_0 is expected to be non-zero and positive for realistic wave fields. In case of a sinusoidal wave field of amplitude ϕ_L for example, $\omega_B(W)$, $\bar{u}'(W)$, and their derivatives can be expressed analytically:

$$\omega_B(W) = \omega_{B,\text{deep}} \frac{\pi}{2} \frac{1}{K(\mu)}, \tag{B25}$$

$$\frac{d\omega_B(W)}{dW} = \frac{\omega_{B,\text{deep}}}{e\phi_L} \frac{\pi}{8} \frac{E(\mu) + (\mu-1)K(\mu)}{\mu(\mu-1)K^2(\mu)}, \tag{B26}$$

$$\bar{u}'(W) = \frac{2\Delta v_t}{\pi} \left[E(\mu) + (\mu-1)K(\mu)\right], \tag{B27}$$

$$\frac{d\bar{u}'(W)}{dW} = \frac{\Delta v_t}{e\phi_L} \frac{K(\mu)}{2\pi}, \tag{B28}$$

with $\mu = (W + e\phi_L)/(2e\phi_L)$, $K(\mu) = \int_0^{\pi/2} d\theta (1 - \mu \sin^2\theta)^{-1/2}$ and $E(\mu) = \int_0^{\pi/2} d\theta (1 - \mu \sin^2\theta)^{+1/2}$ the complete elliptic integrals of the first and second kind respectively, $\omega_{B,deep} = k_L(e\phi_L/m)^{1/2}$ the deeply trapped bounce frequency, and $\Delta v_t = 2(e\phi_L/m)^{1/2}$ the velocity

trapping width. From relations (B25)-(B28), one then obtains the following estimate for α:

$$\alpha(W) = -\frac{\bar{u}'}{\omega_B}\frac{d\omega_B}{dW}\left(\frac{d\bar{u}'}{dW}\right)^{-1} = \frac{\left[E(\mu)+(\mu-1)K(\mu)\right]^2}{\mu(1-\mu)K^2(\mu)}. \tag{B29}$$

Relations (B25), (B27), and (B29) for the bounce frequency ω_B, x-averaged velocity $\bar{u}'$, and parameter α as a function of the energy level W have been plotted in Fig. 18.

A more advanced form of the Dodin model would be to account for a true, non-singular distribution of trapped particles over a finite energy interval $W_{\max} < W < W_c$, with $W_c < W_{\max}$. Assuming a sinusoidal wave for convenience, one can make use of equations (B25)-(B29) to evaluate the coupling coefficient $C_D = -\chi^t_{n,n'}$ given by (B21). As relations (B25)-(B29) are expressed with respect to W (or effectively μ), one changes the integration variable in (B21) from J to W (or μ) which leads to

$$\begin{aligned} C_D &= \omega_p^2 \int_{W_{\min}}^{W_c} dW \frac{d\bar{u}'}{dW}\frac{2f_L/N}{\delta\omega_S'^2-\omega_B^2}\left(1-\frac{2\,\alpha\,\omega_B^2}{\delta\omega_S'^2-\omega_B^2}\right) \\ &= \omega_p^2 \int_0^{\mu_c} d\mu \frac{d\bar{u}'}{d\mu}\frac{2f_L/N}{\delta\omega_S'^2-\omega_B^2}\left(1-\frac{2\,\alpha\,\omega_B^2}{\delta\omega_S'^2-\omega_B^2}\right), \end{aligned} \tag{B30}$$

with $d\bar{u}'/d\mu = \Delta v_t K(\mu)/\pi$ and having furthermore used the relation $\omega_t^2 = \omega_p^2 N_t/N$, expressed J in terms of $\bar{u}'$, come back to the form $f_L(W)$ for the distribution (assumed to be equal to zero for $W > W_c$), as well as defined $\mu_c = (W_c + e\phi_L)/(2e\phi_L)$. According to Eqs. (B25) and (B28), ω_B^{-2} and $d\bar{u}'/dW$ both present logarithmic singularities through the complete elliptic integral $K(\mu)$ in the limit of marginally trapped particle, *i.e.* for $W \to W_{\max} = e\phi_L$, corresponding to $\mu \to 1$. On its own, this logarithmic singularity would be integrable in (B30), assuming f_L finite for $W = W_{\max}$. According to (B29), the parameter α however presents a singularity $1/(\mu-1)$, which is obviously non-integrable. This further illustrates in the case of sinusoidal wave field that the reduced Dodin model is indeed invalid for representing the dynamics of marginally trapped particles and that f_L must therefore be set to zero for $W_c < W < W_{\max}$ ($\mu_c < \mu < 1$).

3. Solution $(\delta k_S, \delta\omega_S') = (0,0)$ to the sideband spectrum

One can prove that in the absence of any approximations, the eigenvalue equation (B9) must admit an eigenmode solution with $\delta\omega_S' = 0$ for $\delta k_S = 0$. According to (B7), this is equivalent to showing that the linearized Vlasov-Poisson system (B5)-(B6) admits a time independent, x-periodic solution $[\delta f(x',v'), \phi(x')]$ with period λ_L.

As the time independent Vlasov-Poisson system (B3)-(B4) for $[f_L(x',v'),\phi_L(x')]$ is translationally invariant with respect to x', $[f_L(x'+\Delta x',v'),\phi_L(x'+\Delta x')]$ is still a solution of this same set of equations for any $\Delta x'$. Inserting this translated solution into (B3)-(B4) and taking the derivative with respect to $\Delta x'$, leads to

$$\left[v'\,\frac{\partial}{\partial x'}+\frac{e}{m}\frac{d\phi_L(x'+\Delta x')}{dx'}\,\frac{\partial}{\partial v'}\right]\frac{\partial f_L(x'+\Delta x',v')}{\partial x'}+\frac{e}{m}\frac{d^2\phi_L(x'+\Delta x')}{dx'^2}\,\frac{\partial f_L(x'+\Delta x',v')}{\partial v'}=0,$$

$$\frac{d^3\phi_L(x'+\Delta x')}{dx^3}=\frac{e}{\epsilon_0}\int dv'\frac{\partial f_L(x'+\Delta x',v')}{\partial x'}.$$

Then, taking $\Delta x'=0$, multiplying the above set of equations by some arbitrary increment $\delta x'$ (only for dimensionality purposes), and identifying $[\delta f(x',v')=\delta x'\partial f_L/\partial x',\delta\phi(x')=\delta x' d\phi_L/dx']$, one obtains:

$$\left[v'\,\frac{\partial}{\partial x'}+\frac{e}{m}\frac{d\phi_L(x')}{dx'}\,\frac{\partial}{\partial v'}\right]\delta f(x',v')=-e\frac{d\delta\phi(x')}{dx'}v'\frac{\partial f_L(W,\sigma)}{\partial W},\tag{B31}$$

$$\frac{d^2\delta\phi(x')}{dx'^2}=\frac{e}{\epsilon_0}\int dv'\delta f(x',v').\tag{B32}$$

Comparing Eqs. (B31)-(B32) to (B5)-(B6), one notices that $[\delta f=\delta x'\partial f_L/\partial x',\delta\phi=\delta x'\partial\phi_L/\partial x']$ is indeed a time-independent, λ_L-periodic solution to the linearized Vlasov-Poisson system, which concludes the proof.

Imposing that the sideband spectra provided by either the reduced KDS or Dodin model still satisfies the property that it contains the solution $(\delta k_S,\delta\omega'_S)=(0,0)$, leads in fact to a condition between the frequency ω_L and wavenumber k_L, *i.e.* to an effective dispersion relation for the LAW. When limiting the Fourier modes composing the sidebands to $n=\pm1$, one obtains the rank 2 system (7)-(8) (with C replaced by C_D for the Dodin model). Assuming that their is an eigenmode with $(\delta k_S,\delta\omega'_S)=(0,0)$, the condition (9) then leads to:

$$\epsilon(+k_L,+\omega_L)\epsilon(-k_L,-\omega_L)=C_D\left[\epsilon(+k_L,+\omega_L)+\epsilon(-k_L,-\omega_L)\right].\tag{B33}$$

Making use of Eq. (12), and neglecting a possible imaginary part of ϵ (related to dissipation), one has $\epsilon(-k_L,-\omega_L)=\epsilon(+k_L,+\omega_L)$ [note this is clearly verified by the fluid relation (2) for ϵ], so that Eq. (B33) becomes:

$$\epsilon(k_L,\omega_L)\left[\epsilon(k_L,\omega_L)-2\,C_D\right]=0.\tag{B34}$$

Naturally, $C_D(\delta\omega'_S)$ must be evaluated here for $\delta\omega'_S=0$. Considering Eq. (B24), resulting from assuming the Dirac distribution $F(J)=\delta(J-J_0)$, Eq. (B34) leads to the following

two possible equations relating ω_L and k_L:

$$\epsilon(k_L, \omega_L) = 0, \tag{B35}$$

$$\epsilon(k_L, \omega_L) = -2(1 + 2\alpha_0)\frac{\omega_t^2}{\omega_{B,0}^2}. \tag{B36}$$

Equation (B35) corresponds to the linear dispersion relation for EPWs, and for ϵ given by (2), leads to the Bohm-Gross dispersion relation (4). Equation (B36) however includes an effective non-linear correction term related to the fraction of particles trapped in the LAW and yields the relation

$$\omega_L^2 = \frac{\omega_{pe}^2}{1 + 2(1 + 2\alpha_0)\omega_t^2/\omega_{B,0}^2} + 3(kv_{\mathrm{th,e}})^2. \tag{B37}$$

As already pointed out in Ref. [12], equation (B36) is in fact equivalent (for $\alpha_0 = 0$) to the non-linear dispersion relation obtained through a separate derivation in Ref. [16] (but under the same assumption of deeply trapped particles as considered in the KDS model and in this sense consistent). Note that this analysis does not determine which of the two dispersion relations (B35) or (B36) is in fact the most appropriate.

---

[1] S. Brunner and E. J. Valeo, Phys. Rev. Lett. **93**, 145003 (2004).

[2] A. Friou, D. Bénisti, L. Gremillet, E. Lefebvre, O. Morice, E. Siminos, and D. J. Strozzi, Phys. Plasmas **20**, 103103 (2013).

[3] L. Yin, B. J. Albright, K. J. Bowers, W. Daughton, and H. A. Rose, Phys. Rev. Lett. **99**, 265004 (2007).

[4] L. Yin, B. J. Albright, K. J. Bowers, W. Daughton, and H. A. Rose, Phys. Plasmas **15**, 013109 (2008).

[5] L. Yin and B. J. Albright and H. A. Rose and K. J. Bowers and B. Bergen and D. S. Montgomery and J. L. Kline and J. C. Fernandez, Phys. Plasmas **16**, 113101 (2009).

[6] K. L. Baker, R. P. Drake, B. S. Bauer, K. G. Estabrook, A. M. Rubenchik, C. Labaune, H. A. Baldis, N. Renard, S. D. Baton, E. Schifano, A. Michard, W. Seka, and R. E. Bahr, Phys. Rev. Lett. **77**, 67 (1996).

[7] J. P. Palastro, E. A. Williams, D. E. Hinkel, L. Divol, and D. J. Strozzi, Phys. Plasmas **16**, 092304 (2009).

[8] W. L. Kruer, J. M. Dawson, and R. N. Sudan, Phys. Rev. Lett. **23**, 838 (1969).

[9] S. Brunner, E. Valeo, B. Still, R. Berger, D. Strozzi, E. Williams, and J. Hittinger, *Documentation to the SAPRISTI code for kinetic simulations of laser plasma interaction*, LLNL report (2008).

[10] R. L. Berger, S. Brunner, T. Chapman, L. Divol, C. H. Still, and E. J. Valeo, Phys. Plasmas **20**, 032107 (2013).

[11] C. Z. Cheng and G. Knorr, J. Comp. Phys. **22**, 330 (1976).

[12] I. Y. Dodin, P. F. Schmit, J. Rocks, and N. J. Fisch, Phys. Rev. Lett. **110**, 215006 (2013).

[13] M. V. Goldman, Phys. Fluids **13**, 1281 (1970).

[14] I. B. Bernstein, J. M. Greene, and M. D. Kruskal, Phys. Review **108**, 546 (1957).

[15] R. L. Dewar, Physics of Fluids **15**, 712 (1972).

[16] M. V. Goldman and H. L. Berk, Phys. Fluids **14**, p. 801 (1971).

[17] G. J. Morales and T. M. O'Neil, Phys. Rev. Lett. **28**, 417 (1972).

[18] T. Chapman, R. L. Berger, S. Brunner, and E. A. Williams, Phys. Rev. Lett. **110**, 195004 (2013).

[19] T. Chapman, S. Brunner, J. W. Banks, R. L. Berger, B. I. Cohen, and E. A. Williams, Physics of Plasmas **21**, 042107 (2014).

[20] D. Bénisti and L. Gremillet, Physics of Plasmas **14**, 042304 (2007).

[21] R. R. Lindberg, A. E. Charman, and J. S. Wurtele, Physics of Plasmas **14**, 122103 (2007).

[22] J. W. Banks and J. A. F. Hittinger, IEEE Trans. Plasma Sci. **38**, 2198 (2010).

[23] S. Brunner, R. L. Berger, J. W. Banks, B. I. Cohen, T. Chapman, J. A. F. Hittinger, W. Rozmus, D. J. Strozzi, B. J. Winjum, and E. J. Valeo, *"Kinetic Simulations of Electron Plasma Waves: trapped electron filamentation and sideband instabilities"*, 54^{th} Annual Meeting of the APS Division of Plasma Physics, Providence, Rhode Island (2012). Abstract ID: BAPS.2012.DPP.CP8.95.

Prepared by LLNL under Contract DE-AC52-07NA27344.